# EFFECT OF WING HEATING ON FLOW STRUCTURE OF LOW SWEPT DELTA WING

A THESIS SUBMITTED TO
THE GRADUATE SCHOOL OF NATURAL AND APPLIED SCIENCES
OF
MIDDLE EAST TECHNICAL UNIVERSITY

BY

GİZEM ŞENCAN

IN PARTIAL FULFILLMENT OF THE REQUIREMENTS
FOR
THE DEGREE OF MASTER OF SCIENCE
IN
MECHANICAL ENGINEERING

DECEMBER 2016

Approval of the thesis:

**EFFECT OF WING HEATING ON FLOW STRUCTURE OF LOW SWEPT DELTA WING**

submitted by **GİZEM ŞENCAN** in partial fulfillment of the requirements for the degree of **Master of Science in Mechanical Engineering Department, Middle East Technical University** by,

Prof. Dr. Gülbin Dural Ünver _____
Dean, Graduate School of **Natural and Applied Sciences**

Prof. Dr. R. Tuna Balkan _____
Head of Department, **Mechanical Engineering**

Assoc. Prof. Dr. Mehmet Metin Yavuz _____
Supervisor, **Mechanical Engineering Dept., METU**

Assoc. Prof. Dr. Almıla Güvenç Yazıcıoğlu _____
Co- Supervisor, **Mechanical Engineering Dept., METU**

**Examining Committee Members:**

Prof. Dr. Kahraman Albayrak _____
Mechanical Engineering Dept., METU

Assoc. Prof. Dr. Mehmet Metin Yavuz _____
Mechanical Engineering Dept., METU

Assoc. Prof. Dr. Almıla Güvenç Yazıcıoğlu _____
Mechanical Engineering Dept., METU

Asst. Prof. Dr. Fatma Nazlı Dönmezer Akgün _____
Mechanical Engineering Dept., METU

Asst. Prof. Dr. Özgür Uğraş Baran _____
Mechanical Engineering Dept., TEDU

**Date:** 28.12.2016

**I hereby declare that all information in this document has been obtained and presented in accordance with academic rules and ethical conduct. I also declare that, as required by these rules and conduct, I have fully cited and referenced all material and results that are not original to this work.**

Name, Last name: Gizem Şencan

Signature:

# ABSTRACT


EFFECT OF WING HEATING ON FLOW STRUCTURE OF LOW SWEPT DELTA WING

Şencan, Gizem

M.S., Department of Mechanical Engineering

Supervisor: Assoc. Prof. Dr. Mehmet Metin Yavuz

Co-supervisor: Assoc. Prof. Dr. Almıla Güvenç Yazıcıoğlu

December 2016, 88 pages

Micro Air Vehicles (MAVs), Unmanned Air Vehicles (UAVs) and Unmanned Combat Air Vehicles (UCAVs), which can be represented by simplified planforms including low swept delta wings, have many advantages in defense industry and aeronautical field. Thus, the aerodynamics of nonslender delta wings including development and application of different flow control techniques have been of considerable interest in recent years.

In this study, it is aimed to investigate the effect of heating on the flow structure over a $35°$ swept delta wing. By applying uniform heat flux from the suction side of the wing, which represents the top surface of the wing, the flow structure has been investigated using Particle Image Velocimetry (PIV) techniques for the cross flow plane at the chordwise distance of $x/C = 0.6$ in a low speed wind tunnel. The velocity measurements are conducted for the attack angles of $\alpha = 4°, 7°, 10°, 13°$ at Reynolds numbers of $Re = 3000$, $Re = 8000$ and $Re = 10000$.

The results indicate that applying uniform heat flux from the suction side of the wing planform does not produce considerable variation on the overall flow pattern within the operational ranges tested in the current study.

The effects are limited to low Reynolds number cases with indicating different behaviors for vortex dominated and pre-stall regimes such that for the attack angles $\alpha = 4°$ and $\alpha = 7°$ the wing heating causes drop in vorticity levels with shifting the concentrations toward the center of the planform, whereas at $\alpha = 10°$ the movement of vorticity concentrations toward the leading edge of the planform with increase in levels is witnessed. Further studies are needed to extend the operational ranges and to draw concrete conclusions regarding the effect of heating on flow structure of low swept delta wing.

**Keywords:** Delta wing, Low sweep, stall, flow control, thermal actuators.

# ÖZ

KANAT ISITMASININ DÜŞÜK OK AÇILI DELTA KANAT ÜZERİNDEKİ AKIŞ YAPISINA ETKİSİ

GİZEM ŞENCAN
Yüksek Lisans, Makina Mühendisliği Bölümü
Tez Danışmanı: Doç. Dr. Mehmet Metin Yavuz
Yardımcı Tez Danışmanı: Doç. Dr. Almıla Güvenç Yazıcıoğlu

Aralık 2016, 88 sayfa

Düşük ok açılı kanatları içine alan basitleştirilmiş planformlar olarak belirtilen Mikro Hava Araçları, İnsansız Hava Araçları ve İnsansız Savaş Araçları savunma sanayisi ve havacılık alanında çok sayıda avantaja sahiptir. Dolayısıyla, farklı kontrol tekniklerinin geliştirilmesi ve uygulanmasını kapsayan düşük ok açılı delta kanatların aerodinamiği son yıllarda önemli ölçüde ilgi çekici bir hal almıştır.

Bu çalışmada, ısıtmanın $35°$ süpürme açılı delta kanat üzerinde oluşan akış yapısına olan etkisinin incelenmesi amaçlanmıştır. Delta kanadın üst yüzeyini temsil eden emme yüzeyinden sabit ısı akısı uygulanmasıyla, akış yapısı parçacık görüntülemeli hız ölçüm tekniği kullanılarak, çapraz akış düzlemi, veter uzaklığı $x/C = 0.6$ 'da düşük hızlı bir rüzgar tünelinde incelenmiştir. Hız ölçümleri hücum açıları $\alpha = 4°, 7°, 10°, 13°$ Reynolds sayısı değerleri $Re = 3000$, $Re = 8000$ ve $Re = 10000$ için gerçekleştirilmiştir.

Elde edilen sonuçlar kanat planformunun emme yüzeyinden üniform ısı akısı uygulamasının, bu çalışmada test edilen çalışma aralıklarında genel akış yapısı üzerinde belirgin değişiklik oluşturmadığını göstermiştir.

Etkiler girdap yapısının baskın ve perdövites öncesi durumları için farklı davranışlar göstererek, düşük Reynolds sayısı durumlarıyla sınırlanmıştır. Öyle ki kanadın ısıtılması, hücum açıları $\alpha = 4°$ ve $\alpha = 7°$ için çevrinti değerlerinde azalmaya neden olarak yoğunluk bölgesini kanadın simetri eksenine doğru kaydırırken, hücum açısı $\alpha = 10°$ için çevrinti yoğunluklarının hareketi hücum kenarına doğru olup, değerlerde artış gözlemlenmiştir. Isıtmanın düşük ok açılı delta kanat üzerindeki akış yapısına etkisine ilişkin çalışma aralığını genişletmek ve somut sonuçlar çizebilmek için ileriki çalışmalara ihtiyaç duyulmaktadır

**Anahtar kelimeler:** Delta kanat, düşük süpürme açısı, üç boyutlu yüzey ayrılması, akış kontrolü, termal aktüatörler.

*To my parents*

## ACKNOWLEDGEMENTS

I would like to express my sincerest appreciation to my supervisor Dr. M. Metin Yavuz for his unique guidance, encouragement, support, criticism and invaluable supervision. It was an honor for me to study with him throughout my graduate education.

I would like to express my deepest gratitude to my thesis co-supervisor, Dr. Almıla Güvenç Yazıcıoğlu, for her encouragement and support. I am also grateful for sharing her valuable experiences in the experimental field.

I would like to express my deepest appreciation to my parents Neşe and Aşkın Şencan for their unconditional love and support in all aspects of my life. This thesis would not have been possible without them and their support.

I owe my sincere acknowledgement to Dr. Habib Umur from Uludağ University to make a contribution to explore my interest on fluid mechanics. And also I would like to thank to Dr. Kahraman Albayrak for sharing his valuable experiences in the experimental fluid mechanics field.

This thesis could not be as improved as it is now without the help and support of my dearest friends and colleagues Cenk Çetin, Burak Gülsaçan, Alper Çelik, Ali Karakuş, Mohammad Reza Zharfa, İlhan Öztürk, Gökay Günacar and all other members of the fluid lab. I am also thankful to all members of YogaŞala TT7, especially to Pınar Enginsu and Gökhan Yavuz for their sincere support and guidance in various ways. And also, I would like to thank my dearest friends Gonca Ünal and Çağla Güngör for their precious friendship and moral support.

I would like to show my gratitude to the lab technicians Rahmi Ercan and Mehmet Özçiftçi and heat lab technician Mustafa Yalçın for their invaluable help.

I would also like to express my sincere thanks to Dr. Oğuz Uzol from METU Aerospace Engineering Department and Dr. Özgür Bayer for sharing their experimental apparatus.

## TABLE OF CONTENTS

## LIST OF TABLES

**TABLES**

## LIST OF FIGURES

**FIGURES**

## LIST OF SYMBOLS

| | |
|---|---|
| $\Lambda$ | Sweep angle |
| C | Chord length |
| S | Semi span length |
| A | Angle of attack |
| Re | Reynolds number based on chord length |
| $U_\infty$ | Free stream velocity |
| **V** | Velocity vector |
| U | Streamwise velocity |
| $\Omega$ | Vorticity |
| $\Psi$ | Streamfunction |
| X | Chordwise distance from wing apex |
| Y | Spanwise distance from wing root chord |
| F | Frequency |
| St | Dimensionless frequency |
| $p$ | Static pressure |
| $C_p$ | Dimensionless pressure coefficient |
| $P$ | Fluid density |
| $N$ | Fluid kinematic viscosity |
| N | Number of samples in a measurement |
| $C_\mu$ | Momentum coefficient |
| $C_L$ | Lift coefficient |
| T | Time |
| $T_\infty$ | the ambient temperature |
| $T_s$ | the temperature of the heated wing surface |
| $T_f$ | the film temperature |
| H | Convective heat transfer coefficient |
| Q | the amount of heat transferred |

| | |
|---|---|
| V | Voltage |
| I | Ampere |
| Nu | Nusselt number |
| PIV | Particle Image Velocimetry |
| Δa | the error taken from thermocouples |
| Δb | the error of the data logger |
| Δz | the total error |
| $\omega_i$ | Uncertainty estimate of a variable i |
| $u_i$ | Relative uncertainty estimate |

# CHAPTER 1

# INTRODUCTION

Unmanned Air Vehicles (UAVs) and Micro Air Vehicles (MAVs) have many advantages in the defense industry and the field of aeronautics. As a result, the aerodynamics of these vehicles has been of considerable interest in recent years. Figure 1.1 illustrates some examples of MAV and UAV designs, which have simple delta wing planforms or blended delta wing-body configurations. According to Gursul [1], all these configurations, which have vortex-dominated flows, suffer from serious stability, aerodynamic, and control problems.

Delta wings are non-traditional wing planforms that can generally be separated into two groups such as slender and nonslender wings according to their sweep angles. As stated in Gursul et al. [2][3][4], the slender wings have a leading edge sweep more than $55°$, while nonslender wings have leading-edge sweep less than or equal to $55°$. Figure 1.2 shows the characteristic dimensions and the sweep angle on a delta wing.

The flow over a delta wing can be described as a pair of counter-rotating leading edge vortices (LEV's). The flow separates from the leading edge of the wing forms as free shear layer that rolls up into a core to form a counter rotating vortices that is stated by Gursul et al. [4]. At sufficiently high angles of attack these LEV's are dominant on slender wings [2]. Vortical flows on a delta wing are shown as a sketch in Figure 1.3. Very low pressures in the vortex core along with high axial velocities result in vortex lift on the delta wing which increases with wing sweep angle [5]. This additional lift force is an important parameter for design of these vehicles [5].

According to Earnshaw and Lawford [6], the maximum lift coefficients and stall angles of nonslender wings are lower than the ones in slender planforms illustrated in Figure 1.4 that shows the dependence of lift coefficient with varying sweep angle. Different forms of unsteady phenomena are observed on delta wings involving vortex breakdown, fluid structure interactions and shear layer instabilities [3]. By increasing attack angle, the jet like core flow stagnates and undergoes a sudden expansion which is called as vortex breakdown and the formation of these dispersed structure is commonly affected by swirl level and pressure gradient [5]. A typical occurrence of vortex breakdown on a nonslender delta wing with sweep angle of $\Lambda = 35°$ is shown in Figure 1.5.

Flow reattachment, that can be simply define as attachment of the separated flow from the leading edges to the wing surface is among the significant features of delta wings. Reattachment does not exist beyond very low attack angles for slender delta wings [5]. While, separated shear layers from the leading edge reattached to the wing surface on nonslender delta wings forming a bound that may even occur after the vortex breakdown [2]. The schematic streamline patterns for reattachment over nonslender wings and with no reattachment on wing surface of slender wings can be seen in Figure 1.6.

The location of the vortex breakdown shifts towards the wing tip with increasing attack angle and the wing is said to be completely stalled when the vortex breakdown location appears at wing apex. For nonslender delta wings, even when vortex breakdown reaches to the apex, primary attachment can take place outboard of the centerline of the wing. This reattachment line moves inboard of the symmetry plane by increasing angle of attack. First, with increasing attack angle the substantial buffeting is occurred within the attachment region. Later with the further increase of the incidence, the observation of attachment corresponds to stall of the wing [3].

The flow over delta wings can be controlled either passively or actively. Especially for low swept delta wing, to delay vortex breakdown and to prevent stall a few alternative flow control techniques have been performed. An example of active flow control technique using thermal actuators is not commonly studied in the literature.

### 1.1 Motivation

The flow over Micro air vehicles (MAV), Unmanned Air Vehicles (UAV) and Unmanned Combat Air Vehicles (UCAV) can be represented by simplified nonslender delta wing planforms. These vehicles experiencing steady flight and/or defined maneuvers generate complex flow patterns which must be well understood for the optimization of flight performances including lift enhancement and buffet loading reduction.

According to previous studies, low sweep angle delta wings have unique flow patterns of leading edge vortices, vortex breakdown and stall. In literature, very few studies are focused on the effects of Reynolds number and attack angles on flow structure in detail. Thus, the characterization of flow structure on low swept wings for different range of Reynolds number and attack angles by using qualitative and quantitative measurement techniques are needed. In addition, the flow over low sweep angle delta wings having sweep angles less than 40° turns to vortex breakdown and three-dimensional surface separation conditions even in low angles of attack [7]. Thus, eliminating three-dimensional surface separation and delaying vortex breakdown over low sweep delta wings are also critical issues. Very few studies investigated alternative flow control techniques for low swept delta wings to delay vortex breakdown and to prevent stall. Especially, the flow control technique using thermal actuators is not studied in the literature commonly.

## 1.2 Aim of the Study

The purpose of this study is to characterize the flow and investigate the effect of wing heating on flow structure over a 35° swept delta wing using thermal actuators. To control the flow, heating the suction side of the wing is performed by using resistance heat wires as thermal actuators. A quantitative flow measurement technique is used in the study to characterize the flow structure over the delta wing. Particle image velocimetry is used for the quantitative flow measurements. The flow structure of a 35° swept wing and control by steady leading edge blowing were investigated in detail in the previous studies [13]. Thus, thermal actuators are used at different heat rates to examine the ultimate effect of convection heat transfer on flow structure (vortex breakdown and stall) as a new control technique.

## 1.3 Structure of the Thesis

In this thesis, five main chapters are provided. Introductory information about the flow of delta wings and the aim of the study along with the motivation is given in Chapter 1.

Chapter 2 summarizes the previous studies about the flow structure and its control on delta wings. While the main attention is given to the non-slender wings, slender wings are also mentioned briefly.

Chapter 3 includes the measurement techniques used in the study and experimental systems. In addition, details of the flow control set-up are also provided in this chapter.

The results are summarized and discussed in Chapter 4. The results of the cross flow Particle Image Velocimetry (PIV) experiments and the results of temperature measurements are presented.

The conclusions based on the results, including the recommendations for future work are provided in Chapter 5.

Figure 1.1 Current and future Micro Air Vehicles and Unmanned Combat Air Vehicles [3].

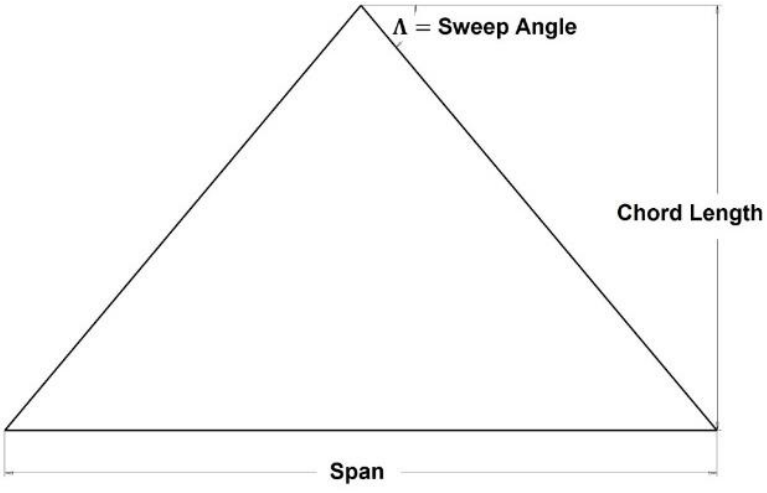


Figure 1.2 Characteristic dimensions and the sweep angle on a delta wing

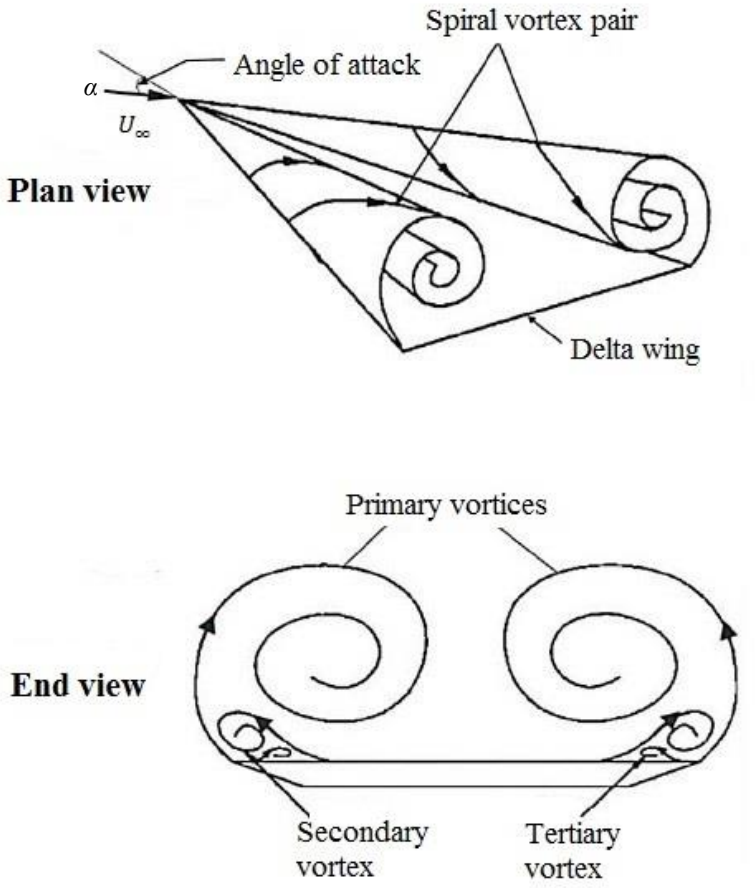


Figure 1.3 Sketch of vertical flows around a delta wing

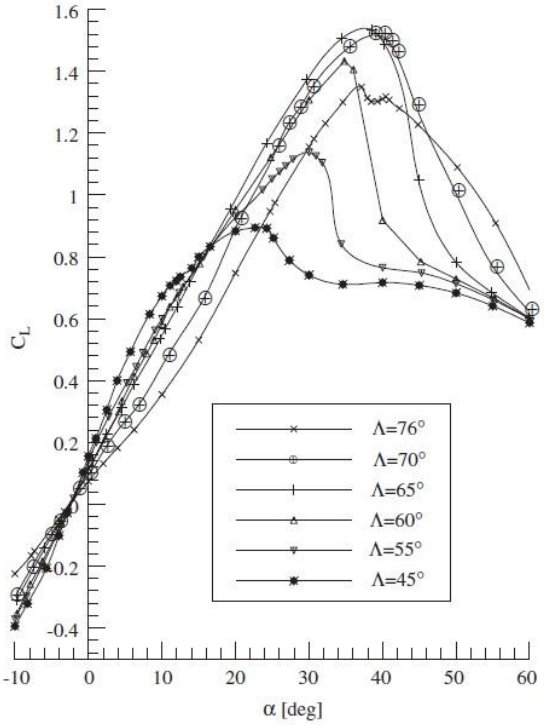


Figure 1.4 Variation of lift coefficient with angle of attack [6]

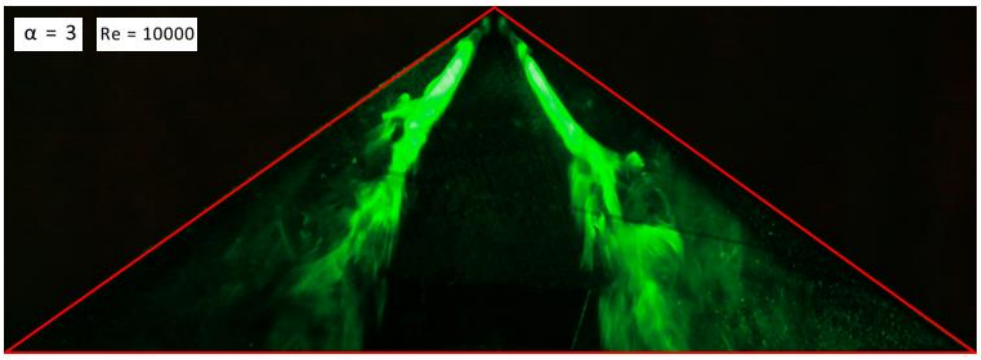


Figure 1.5 Leading-edge vortices and vortex breakdown over 35° −sweep wing [13]

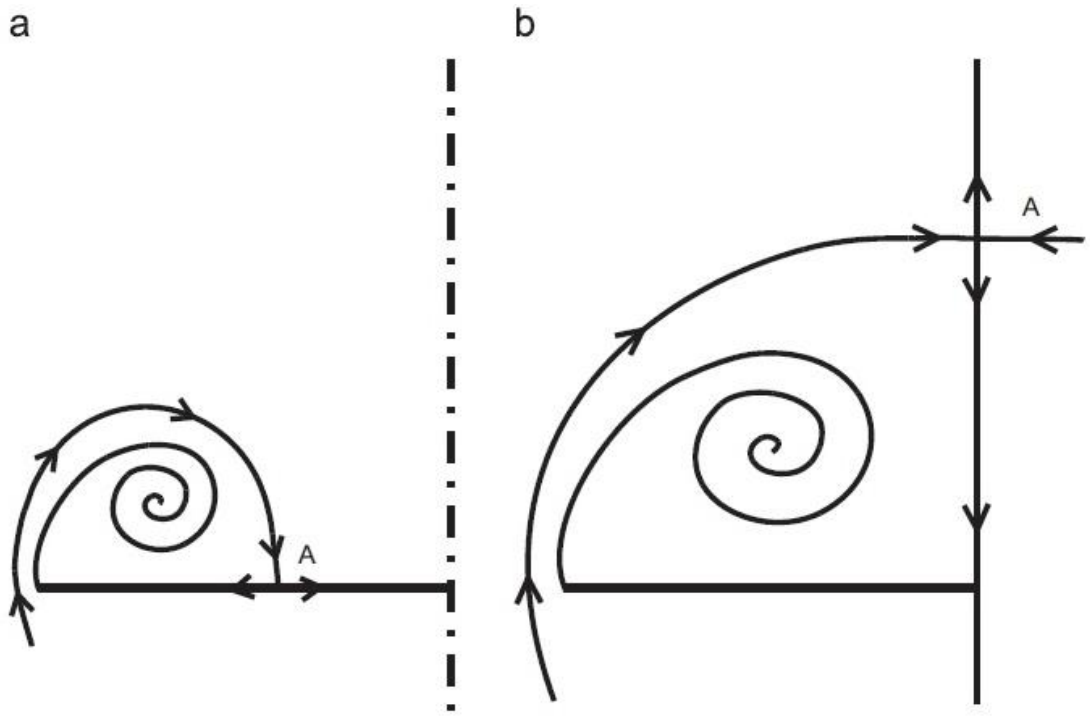


Figure 1.6 Schematic streamline patterns for (a) reattachment over nonslender wings and (b) with no reattachment on wing surface on slender wings [2].

# CHAPTER 2

# LITERATURE REVIEW

In literature, the most studies are focused on high sweep angle delta wings, whereas the knowledge in the structure of flow and their control for low swept wings are very limited. In this chapter, the flow structure over high and low sweep angle wings are summarized. However, the main focus area is on the flow structure and its control for low swept delta wings.

## 2.1 Flow structure on delta wings

A wide range of studies have been performed on delta wings due the subject being an exciting area for researchers for a long time. There are various studies about the flow structure on high swept delta wings, which provides substantial knowledge about the flow structure on these types of wings. Several studies are conducted to understand the aerodynamic characteristics of slender delta wings, vortices, and vortex breakdown. Earnshaw and Lawford [6], Barlett and Vidal [8], Wentz and Kohlman [9], Lee [10] conducted experiments on high sweep delta wings to understand the characteristics of slender delta wings and vortices. Sarpkaya [11], [12],[13] focused on vortex breakdown on swirling flow. Benjamin [14], [15], Hall [16], Escuider [17], Delery [18] and Lucca-Negro [19] conducted several theoretical and experimental studies about vortex breakdown. There are also various researchers which worked on the unsteady phenomena of these flow structures such as Gursul [20], [21], Rockwell [22], Gordnier and Visbal [23], Menke, Yang and Gursul [24]. According to all those studies, there are several unsteady flow phenomena on slender delta wings; such as shear layer

instabilities [25], vortex shedding [26], vortex wandering [27], [28], oscillations of vortex breakdown location [29], [30], and helical mode instability [31]. These unsteady flow structures causes buffeting at aircraft structures such as wings and fins and instability on the aircraft. Besides extensive knowledge about the aerodynamic characteristics of slender delta wings, vortices, vortex breakdown and the unsteady flow structure, the knowledge in the literature about the structure of flow, the unsteady flow structure and control the flow structure is relatively limited for nonslender delta wings having sweep angles less than $40°$.

Different types of flow patterns are observed on low swept delta wings when it is compared to the high swept wings [3]. Several researchers conducted studies to understand the flow structures on low or moderate sweep delta wings. Taylor and Gursul [4] and Taylor, Schnorbus and Gursul [32] performed studies in order to investigate the leading edge vortex cores over $50°$ swept wing. They were conducted their experiments at relatively low Reynold number and attack angle by using dye visualization technique. According to their study, dual vortex structure was obtained in the flow field. Ol and Gharib [33] used a technique of stereo imaging to compare the flow structure on $\Lambda = 50°$ and $\Lambda = 65°$ wings. Yaniktepe and Rockwell [34] conducted water tunnel experiments on a $\Lambda = 38.7°$ delta wing using PIV technique at different angles of attack. The existence of dual vortex structure was also confirmed in the study. Gordnier and Visbal [25] performed computational simulations of the flow over a $\Lambda = 50°$ wing for angle of attack values $\alpha = 5°, 10°$ and $15°$. As it is mentioned in aforementioned studies the vortical structure formed by the separation of the shear layers occurs at low incidences, and forms close to the wing surface.

### 2.2 Shear layer instabilities

The separated shear layers from leading edge roll up into discrete smaller scale vortices to form the primary leading edge vortices. This unsteady behavior of the

shear layer causes a significant wandering of the vortex core around a mean core location. This unsteady flow structure can occur on both low and high swept wings that was first studied by Gad-el-Hak and Blackwelder [35]. They conducted an experiment at low Reynolds number on $\Lambda = 45°$ and $\Lambda = 60°$ delta wings. According to their experiments, vortices were occurred in the shear layer on both wings. This phenomenon was known as Kelvin-Helmholtz type instability that was also represented by Payne et al. [36], Lowson [37] and Gordnier [38] in their studies. Reynolds et al. [39], Ng et al. [40] and Visbal et al. [41], [42] suggest another hypothesis that the interaction between the shear layer and secondary vortex predominantly induce the transverse perturbation of these substructures along the leading edge of the wing. Yavuz et al. [43] was performed an experimental study on a $38.7°$ swept delta wing. According to this study, co-rotating pattern of small scale vorticity concentrations existed in the region of leading edge that is shown in Figure 2.1.

### 2.3 Vortex breakdown

Releasing smoke or dye in the vortex core are common methods to visualize the vortex breakdown especially for the spiral vortex breakdown that occurs on high swept delta wings. According to aforementioned studies, it is known that the vortex breakdown over slender wings is much more abrupt than the vortex breakdown in nonslender wings. Thus, interpreting these streakline visualizations is more challenging in nonslender wings. The comparison of the experimental study [34] for a $39°$ swept wing at $\alpha = 7°$, and the computational study [25] for a $\Lambda = 50°$ wing at $\alpha = 15°$ can be seen in Figure 2.2. Both the numerical and experimental studies represent similar flow pattern for streakline visualizations. In addition, three stages of vortex breakdown were identified by Yaniktepe and Rockwell [34]. The axis of the vortex core just starts to oscillate in the first region. The breakdown onset is represented by initial point of second region where is

dominated by small scale bubbles and/or elongation of the vortex core. This is followed by the stagnation and abrupt expansion of flow in third region. According to the flow visualization experiments, Taylor et al. [32] and Ol and Gharib [33] have expressed that fluctuations of vortex breakdown corresponds to 40% to 50% location of the chord length are obtained in the streamwise direction. Several studies have been performed in detail over a $\Lambda = 50°$ wing both experimentally [39],[40],[44], [45] and numerically [25] to understand the structure of the vortex breakdown. Figure 2.3a and 2.4 illustrate the vortex breakdown effect on flow at angle of attack $\alpha = 15°$. The high suction peaks are observed at upstream locations and they are not significant at downstream which can be seen in Figure 2.4. In addition, the primary vortex core is observed more expended and the size of the vortex increases. Figures 2.3b and 2.3c compare the structure of the vortex in detail included the downstream and upstream of vortex breakdown.

### 2.4 Shear layer reattachment and stall

Attachment of the shear layer close to the centerline of the wing is a distinct feature for nonslender delta wings. Several studies were conducted for nonslender delta wings such as that by Taylor and Gursul [44]. They performed an experimental study on $50°$ sweep delta wing for $\alpha = 10°$ and $25°$, using PIV measurements to investigate the reattachment process. The measurements were conducted in a plane parallel and adjacent to the surface of the wing. Figure 2.5 shows PIV measurements of the streamline pattern and rms value of velocity. At the lower incidence, leading edge vortices occurs. The primary reattachment line shifts towards the midplane of the wing by increasing attack angle. For $\alpha = 15°$, the maximum velocity fluctuations occur after the vortex breakdown point, under the vortex axis. When angle of attack reaches $\alpha = 20°$, difference of the nature of the fluctuation can be observed and the vortex breakdown reaches the apex. The

largest fluctuations occur near the wing centerline in the region of the apex. An additional source of buffeting is caused by the interaction between these large fluctuations and the shear layer reattachment for nonslender delta wings. For the highest attack angle for this study, the fluctuations of the velocity are obtained very low near the surface and the wing has stalled. Gursul et al. [45] performed experiments both in water and wind tunnel. According to the experiments, the attachment line shifts toward the centerline. In the wind tunnel experiment, it finally reaches the midplane corresponds to pre-stall condition at $\alpha \approx 22 - 23°$. By increasing attack angle to $\alpha = 25°$, stall condition is observed and swirling patters are occurred. In Figure 2.6, the spanwise location of reattachment line varied with attack angle is depicted.

### 2.5 Control of Flow Structure on Delta Wings

It is known that delta wings usually have stability and flight control problems due to not having regular aerodynamic control surfaces. Thus, for improving the flight performance and stability of air vehicles and reducing the effects of the unsteady loading on structures such as wings and fins, different types of techniques have been conducted. The main purposes on control of delta wings are delaying or preventing vortex breakdown and vortex instabilities, elimination of three-dimensional surface separation, controlling vortex formation and flow reattachment, and increasing the lift. Control of flow is generally divided into two main groups, as passive and active control of the flow structure. In passive flow control, no energy input and feedback mechanism is required. Passive control can be applied by using different material and surfaces of wings such as flexible delta wings or variable-sweep, and adding control surfaces to the wing such as leading edge flaps, strakes, and canards. However, in active control, an energy input is needed to manipulate the flow over the wing. Several applications of active control can be conducted such as blowing and suction from different regions of

wing, piezoelectric and acoustic excitation, and small and large scale perturbations.

### 2.5.1 Passive control

Passive control methods used to manipulate the flow over a delta wing are highly dependent on the type of the wing due to the presence of different flow structures over slender and nonslender delta wings.

Flow control methods aiming to control the vortex breakdown over slender delta wings have an important place among the other methods. According to Gursul et al. [46] and Mitchell et al. [47] several passive control techniques can be applied to control the breakdown of a vortex on slender delta wings such as apex flaps, canards, leading edge flaps and extensions. Klute et al. [48] conducted to a study on a delta wing to understand apex flap effect on the flow structure. According to their results, when the flap was bended and stationary, the vortex breakdown was delayed on both cases. They also found that when the apex flaps bended with an angle toward negative direction, the maximum delay occurred. Myose et al. [49] performed a study to determine the effect of 60-degree swept canard on the vortex breakdown location. They found that when the position of the canard reached to the original wing, the delay of vortex breakdown could be observed. In addition, the delay of three-dimensional surface flow separation was observed that corresponds to 19% delay in stall angle. Another study was conducted by Lynn and Gursul [50] that investigated LEV's and vortex breakdown on a $65^{\circ}/65^{\circ}$ tandem wing planform that is shown in Figure 2.7. According to results, vortex breakdown development was delayed with the application of the planform. This planform exhibits a considerable delay in the development of vortex breakdown when it was compared to a main delta wing in similar conditions. For nonslender delta wings, Gursul et al. [46] stated that the most effective method is the one that aims reattachment of the flow to the wing surface. Only by using this method, the

flexibility of the wing increases over a nonslender delta wing. According to Mitchell and Delery [47], increasing the flexibility of the wing or applying additional control surfaces are the most efficient passive control techniques over nonslender wings. In addition, Vardaki et al. [51] investigated the effect of buffeting over 50° and 60° swept delta wings. They found that only in low sweep angle delta wings, delay in the three-dimensional surface separation and increase in lift force were obtained. Moreover, they also stated that enhancing the lift performance on the delta wing, improving the reattachment of the shear layer, and the excitation of shear layer instabilities were the main parameters. Taylor et al. [52], [53] also performed an experimental study on several delta wings had different sweep angle to investigate the effect of wing flexibility. They also found similar results with Vardaki et al. [51].

### 2.5.2 Active control

Active flow control is performed in several ways. The most common types are blowing and suction, which are commonly used as flow control methods for leading-edge vortices and breakdown. Blowing and suction methods can be divided into different groups such as trailing edge blowing, leading edge blowing and suction, and tangential blowing.

Several studies were conducted for active flow control for slender delta wings. Mitchell et al. [54], Shih et al. [55], and Phillips et al. [56] conducted studies about trailing edge blowing and showed its effectiveness on the flow characteristics and vortex breakdown structure. Vorobieff et al. [57] studied blowing from trailing edge to prevent vortex breakdown. They employed intermittent trailing-edge blowing in their study. Hummel [58] employed suction at the trailing-edge. Wang et al. [59] and Nawrocki [60] was conducted to a study on a delta wing vortices using vectored trailing edge jet. Badran et al. [61] studied suction both from leading edge and the upper surface of a wing. McCormick et al.

[62] investigated the effect of shear layer control on leading edge vortices by suction. The effectiveness of leading-edge suction through a line of holes on both sides of a delta wing was investigated by Maines et al. [63]. Wood et al. [64] performed a study to control the asymmetric vortical flow over delta wings by tangential leading edge blowing. Gad-el-Hak et al. [65] and Gu et al. [66] applied periodic tangential blowing and suction along the leading edge of delta wings. Greenwell et al. [67] conducted a study on a delta wing to understand the effect of asymmetric tangential blowing from the leading edge on roll moment characteristics. In addition to these, Chui et al. [68], [69] used forebody slot blowing technique to control the vortex breakdown over a delta wing. In this study, symmetric and differential blowing were employed. The effect of both passive (canard) and active (blowing) flow control can be seen from their study in Figure 2.8. Another active flow control technique were performed by Deng et al. on a slender delta wing by using oscillating leading-edge flaps [70]. The study indicated that the vortex breakdown significantly depends on the amplitude of the oscillation.

The study about control of flow structure on nonslender delta wings are limited when compared to high swept wings. However, the research on active flow control of nonslender delta wings have shown an increase in recent years. Wang et al. [71] performed blowing from the trailing edges to determine the effects on the wing aerodynamics and leading edge vortices on delta wings with $\Lambda = 50°$ and $\Lambda = 65°$. For the $50-$degree delta wing, the spanwise location of the nozzle highly affects the jet. For the slender wing, the lift force increases significantly with the undervortex blowing near the stall angle and in the post-stall region. At low angles of attack, the effect of blowing on the breakdown location and reattachment is low, and the highest effects appear near the stall and in the post-stall region. Jiang et al. [72] employed unsteady trailing-edge blowing on $50-$and-$65-$degree sweep delta wings in water tunnel. Flow visualization, force

and velocity measurements were implemented at stall and post-stall incidences. Yavuz et al. [73] applied steady trailing-edge blowing on a $35-$degree sweep delta wing to prevent three-dimensional separation on the wing surface. This technique had influence on the surface patterns located well upstream. At high angles of attack, three-dimensional surface separation was destroyed near the apex. Yaniktepe et al. [34] and Vardaki et al. [74] investigate the effect of oscillation on formation of the vortex and reattachment at post-stall regime. According to their results, the totally separated flow can be reattached on oscillating low and moderate sweep delta wings, as shown in Figure 2.9. Williams et al. [75] conducted pressure and PIV measurements on a 50-degree sweep delta wing by performing oscillatory blowing. They observed that the stall is delayed and the upper surface suction force is increased significantly. For the post-stall region, the optimal momentum coefficient increases with the increase of the angle of attack.

### 2.5.3 Control by thermal actuators

Employing thermal actuators to control the flow structure on low swept delta wings is not a very common method. On the other hand, several studies showing the effect of heating on the flow structure over different objects such as triangular planforms, square cylinder, airfoils, etc. have been conducted.

The effect of heating on leading vortices was investigated by Marchman [76]. An aluminum, $60°$ sweep, double delta wing was tested at $Re = 10^6$ for different angle of attack and yaw. The wing could be heated to over $600$ °F and it was possible to reach surface temperatures more than twofold of freestream absolute temperature. According to Figure 2.10, it can be seen that, the ratio of temperature up to two has almost no effect on lift. On the other hand, the heating effect on drag was strong and increased with attack angle. Drag increased up to $25$ % at high attack angles.

That result was consistent with an earlier study of Norton et al. [77] who investigated the effect of surface temperature on a heated NACA0012 airfoil on subsonic stall. They conducted both analytical and experimental studies at $Re = 10^5$ with a uniform temperature distribution over the entire airfoil surface. According to their results, the stall angle of an airfoil is reduced with the increase of temperature. In addition, the maximum lift coefficient $C_L$ is reduced and the drag of an airfoil appears to increase as the wing is heated.

Mabey [78] investigated heat transfer effect on aerodynamics and possible inferences. It was found that heating promotes flow separation and causes a decrease in Reynolds number. On the contrary, the flow separation is delayed by cooling the surface that means an increase in Reynolds number. Moreover, increase in maximum lift to drag ratio is due to an increase in heat flux.

Balle and Breidenthal [79] proposed the persistence theory to explain the relation between the stationarity of vortex and the effect of different heat fluxes across the surface. The rotational and the translational velocities on a vortex are shown in Figure 2.11. According to persistence theory, if the rotational velocity is higher than the translational velocity, the vortex is considered stationary. In addition, the stationary vortex continuously brings in fresh fluid to the interface, and takes out the heated fluid. Thus, it helps to increase heat convection.

Srigrarom et al. [80] also used persistence theory on their study to prevent the vortex breakdown of the delta wing vortices. They performed both wind and water tunnel experiments on a $60-$degree high swept delta wing. They applied the heat flux on the suction side of the delta wing by using a heat lamp and a heat gun. Two different empirical correlations between Nusselt and Reynolds numbers were established for stationary and non-stationary vortex flow case. According to these correlations, Nusselt number was higher in stationary vortex case. Thus, the stationary vortex provides better heat convection than non-stationary vortex.

Kim et al. [81] investigated the aerodynamic efficiency improvement of a small-scale airfoil by surface temperature and heat transfer. They applied the heat flux by heating the lower surface and cooling the upper surface of the airfoil. The computational and theoretical predictions indicated that varying surface temperature does not produce significant effect at full-scale due to having small thickness of thermal and velocity boundary layers compared to the airfoil chord. However, the effect of varying surface temperature was very high at microscale. The variation of lift coefficient with the attack at various Reynolds numbers and surface temperatures is shown in Figure 2.12. At high Reynolds number, the temperature difference between the upper and the lower surface did not have significant effect on lift and stall. However, at low Reynolds number, the temperature difference between the upper and lower surface caused the delay of stall when compared with no temperature difference case.

Bekka et al. [82] used a numerical method to investigate the effect of heat transfer around the small scale airfoil using different turbulence models.

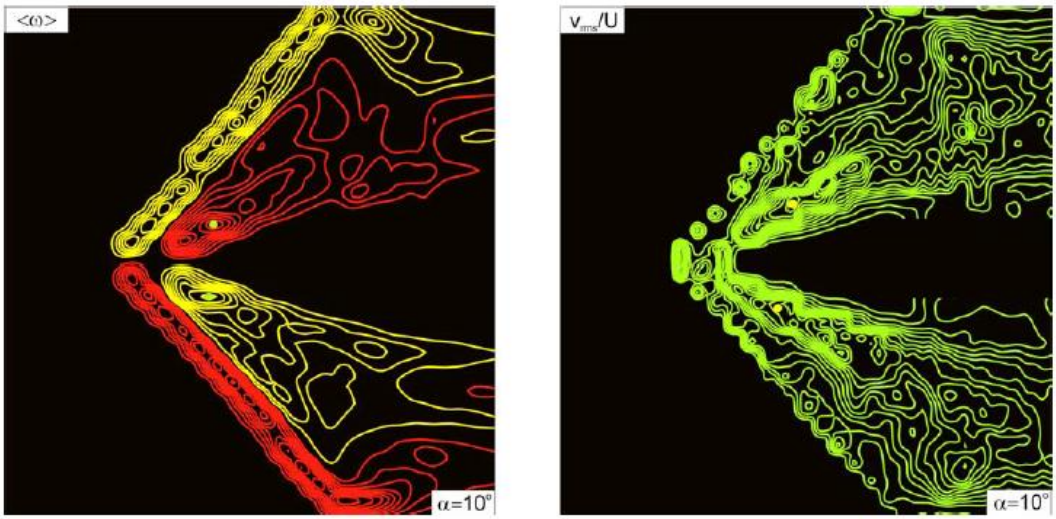


Figure 2.1 Shear layer substructures visible in the PIV measurements of Yavuz et al. [50] for a $\Lambda = 38.7°$ sweep wing on a plane parallel and immediately adjacent to the surface of the wing

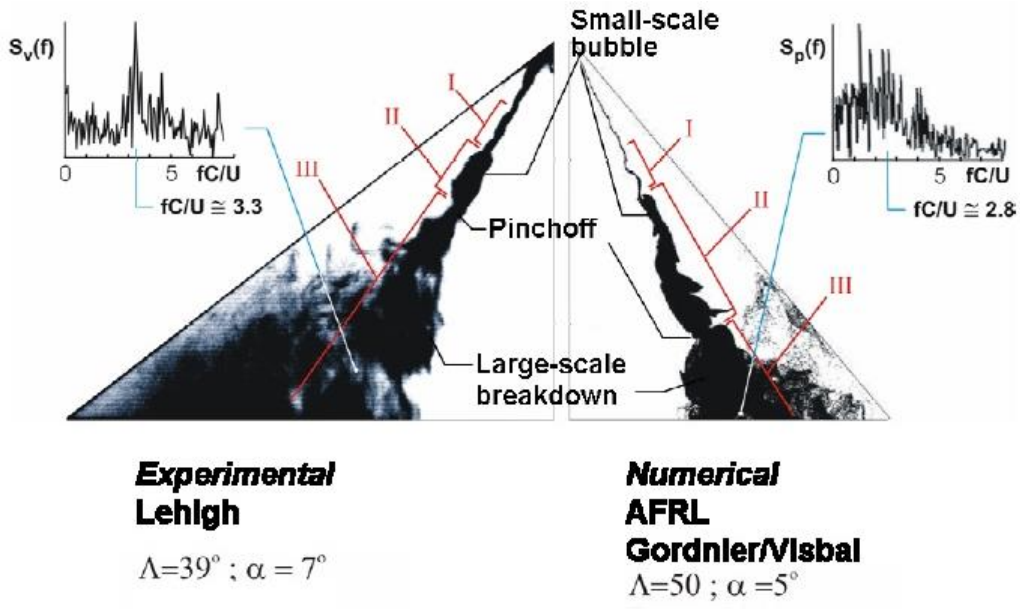


Figure 2.2 Comparison of dye flow visualization of Yaniktepe and Rockwell [41] and the computational streakline of Gordnier and Visbal [16].

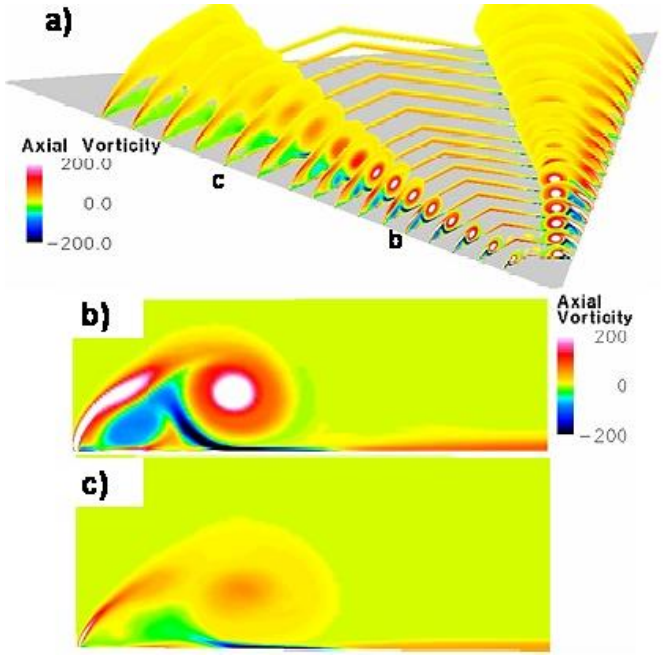


Figure 2.3 Mean vortex structure over a $\Lambda = 50°$ sweep delta wing at $\alpha = 15°$ angle of attack showing vortex structure b) crossplane upstream of breakdown c) crossplane downstream of breakdown [16]

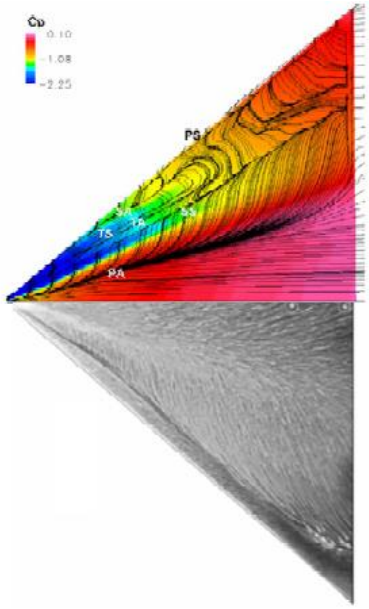


Figure 2.4 $\Lambda = 50°$ sweep wing at $\alpha = 15°$ Upper – Surface streamline pattern and pressure coefficient [16], Lower – Surface oilflow pattern [30]

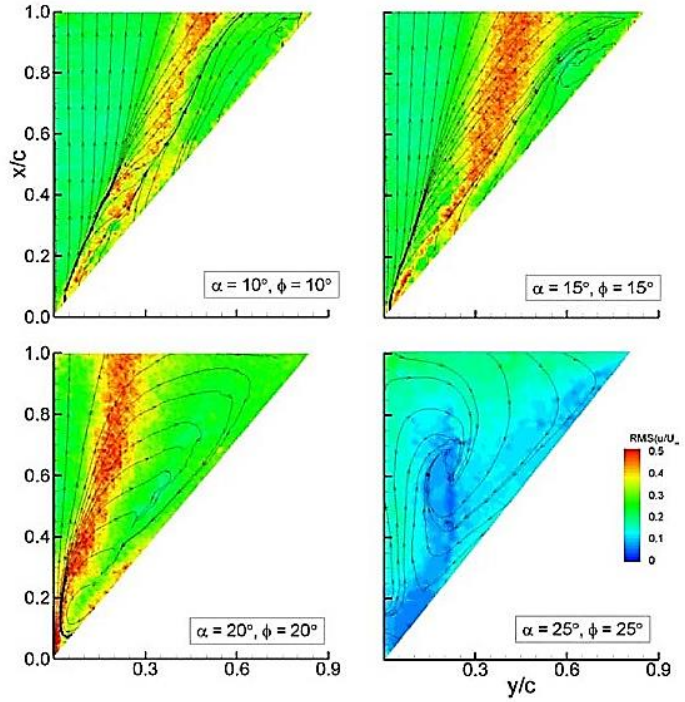


Figure 2.5 PIV measurements [51] of the rms velocity and streamline pattern on a plane parallel and adjacent to the surface of the wing.

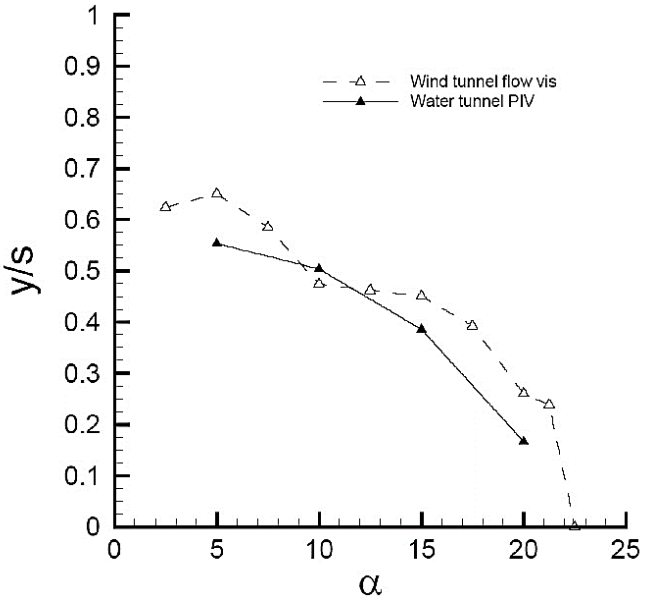


Figure 2.6 Variation of spanwise location of reattachment line with incidence for measurements in both a wind tunnel and a water channel [51]

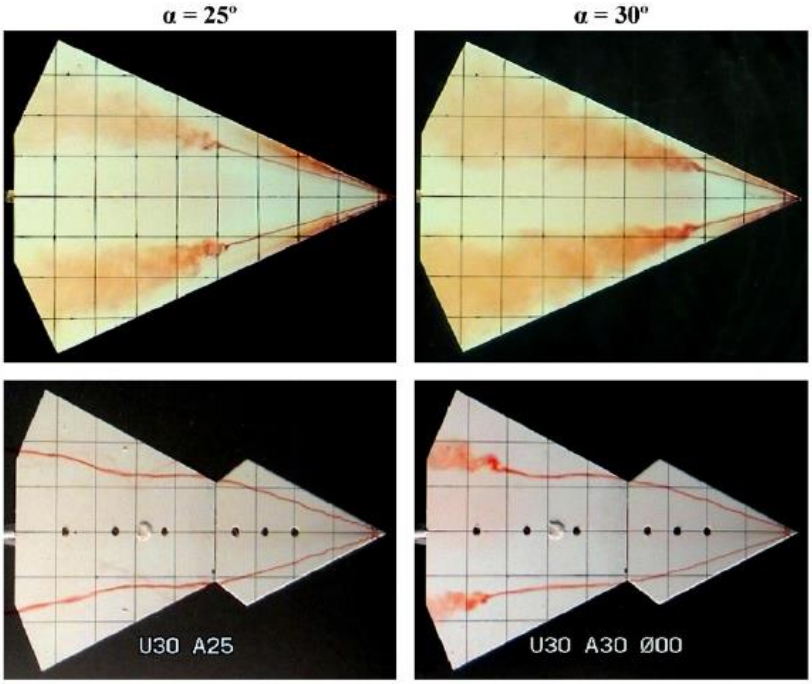


Figure 2.7 Vortices and breakdown for a $65°/65°$ delta wing [56]

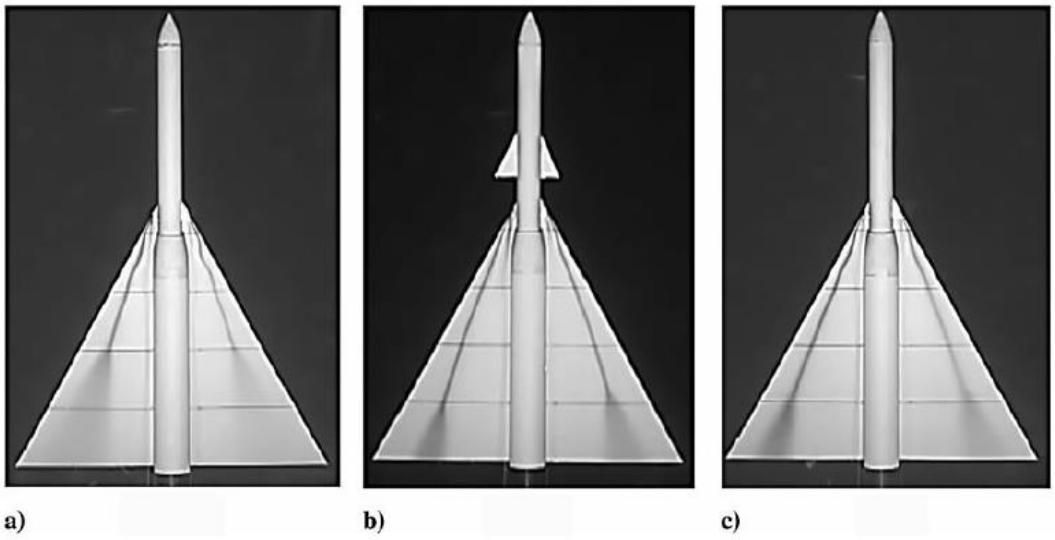


Figure 2.8 Effects of canards and double-sided forebody slot blowing [74] on the vortex breakdown location at $\alpha = 20°$ and $Re = 6.8 \times 10^4$ for a) basic configuration, b) basic configuration with canards, and c) basic configuration with double-sided slot blowing at $C_\mu = 0.2$

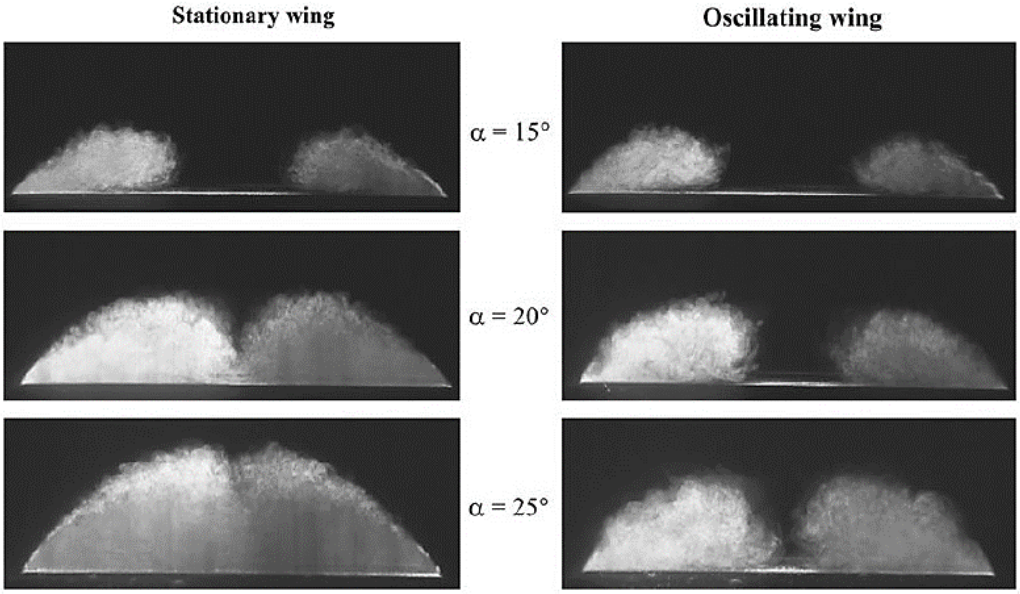


Figure 2.9 Time-averaged laser fluorescence flow visualization [80] for stationary ($Sr = 0$) and oscillating wings ($Sr = 1.0, \Delta\emptyset = 1\ deg$), $\Lambda = 50°$

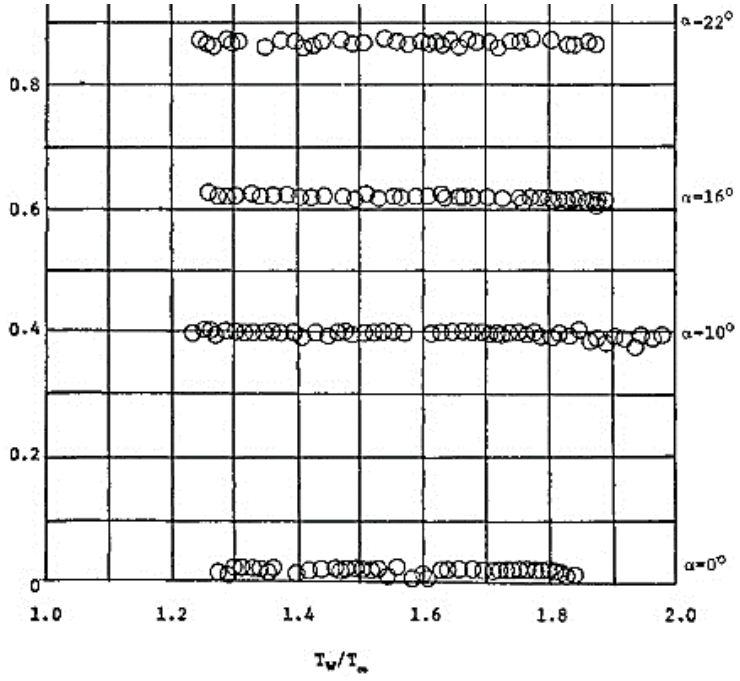


Figure 2.10 Effect of surface temperature on lift, $\beta = 0°$ [81]

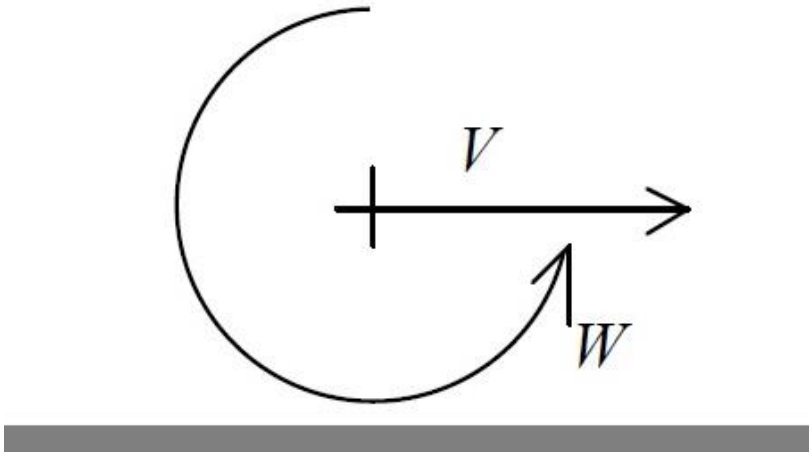


Figure 2.11 Schematic of a vortex near a boundary [84]

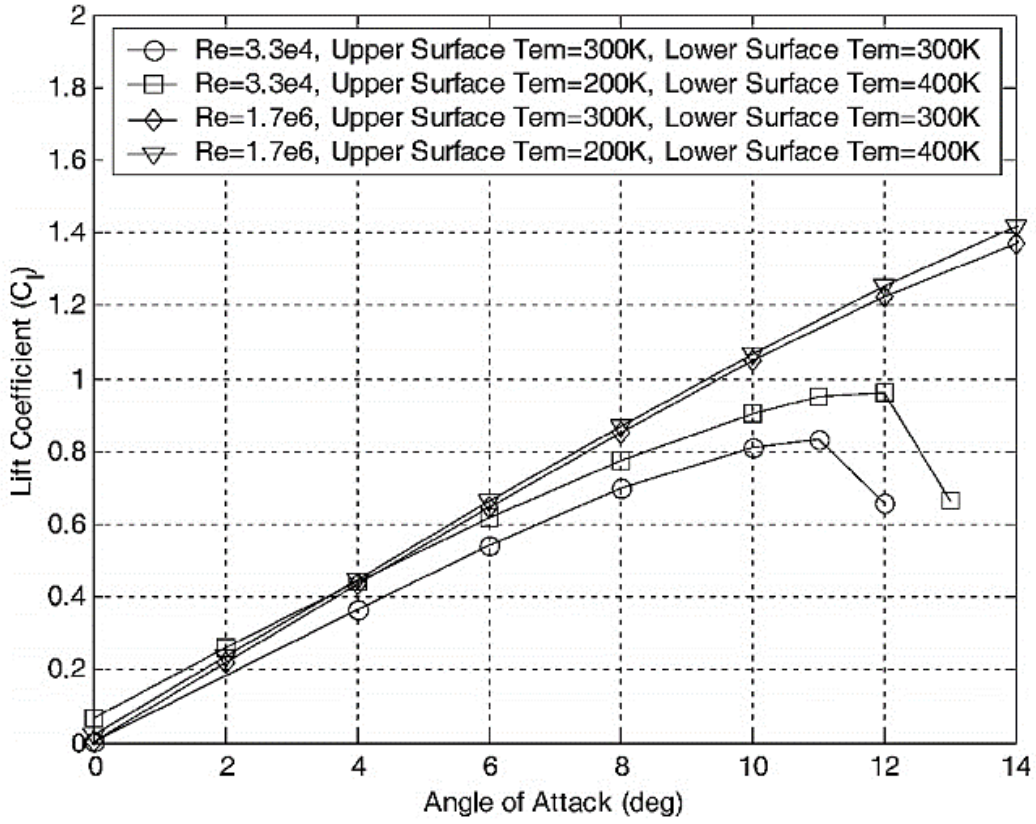


Figure 2.12 Lift coefficient as function of angle of attack at various Reynolds numbers and surface temperatures [86]

# CHAPTER 3

# EXPERIMENTAL SET-UP AND MEASUREMENT TECHNIQUES

## 3.1 Wind Tunnel Facility

An open circuit, low-speed and suction type wind tunnel, located at the Fluid Mechanics Laboratory of the Mechanical Engineering Department at Middle East Technical University, was utilized to conduct the experiments. The wind tunnel, shown in Figure 3.1, consists of five main parts including; settling chamber, contraction, test section, diffuser and driver (fan).

Air enters to the tunnel through two inlet sections. Fine-mesh screens are mounted at both inlets to increase the uniformity of air and to prevent the entrance of any undesired materials. In order to reduce turbulence intensity in the test section and to obtain a more uniform flow field, a honeycomb and three fine grids are used in the settling chamber. The settling chamber, also called entrance section, is 2700 mm long. Contraction section reduces the area and causes significant increase in free stream velocity before entering the test section. It is located between the settling chamber and the test section. The total length of the contraction section is 2000 mm and has the contraction ratio of 8: 1.

A fully transparent, Plexiglas test section is used due to the requirement for optical access for the laser-based velocity measurement technique. The dimensions of the test section are 750 mm width, 510 mm height, and 2000 mm length. The bottom, top and side walls allow access to the inside of the test section to provide a convenient working environment for setting up the experiments. The maximum free stream velocity can be obtained in the test section is 30 m/s.

High speed air that leaves the test section expands through the diffuser section. By decelerating the high-speed flow, static pressure recovery is achieved. Moreover, the power required to run the tunnel facility is reduced by the diffuser. Diffuser is 7300 mm long with a 3° cone angle.

At the exit section of the wind tunnel, a frequency controlled axial fan is used. It can be controlled via a remote control unit to obtain the desired free stream velocity in the test section.

In this study, the free stream velocities, $U_\infty$, are 0.45 m/s, 1.1 m/s and 1.44 m/s corresponding to Reynolds numbers of 3000, 8000 and 10000 based on the chord length, $C$, of the wing, which is calculated as shown in Equation 3.1. Here, $\upsilon$ is the kinematic viscosity of air calculated at the free stream temperature.

$$Re = \frac{U_\infty \cdot C}{\upsilon} \tag{3.1}$$

### 3.1.1 Wind tunnel characterization

The wind tunnel was characterized before the experiments to obtain the required velocities in the test section. Pitot-static tube pressure measurements and Laser Doppler Anemometry (LDA) were used for the characterization. At a wide range of fan powers, the velocity measurements were performed at a predetermined location in the test section. Both inclined manometer and pressure scanner were used in pitot-static tube measurements. Humidity, the ambient temperature, and the geographic elevation of the lab were taken into account in order to calculate velocities from the dynamic pressures obtained from the Pitot-static tube.

Based on the measurements, average velocity and turbulence intensity values were plotted against tunnel power as can be seen in Figure 3.2. The characterization curve was found to be linear for the fan power greater than 4%. The difference in

velocity values between LDA and pitot-static tube measurements was obtained to be around 3% maximum. Moreover, the maximum turbulence intensity value in the test section was recorded as 0.9%.

### 3.2 Wing Model

A delta wing with a sweep angle of $\Lambda = 35°$ was used in the experiments. The chord length and the span of the wing were 105 mm and 300 mm, respectively. The wing was made of aluminum with a thickness of 5 mm and fabricated using CNC machine. It was beveled at an angle of $45°$ from the leading edges on the windward side. CAD drawing of the designed wing model is provided in Figure 3.3. The maximum blockage ratio does not exceed 0.7% at the highest attack angle of $\alpha = 10°$.

The wing was positioned with a mount mechanism in the test section in order to maintain the desired angle of attack, yaw and roll angles without disturbing the upstream flow. The view of the wing, the mount, and the test section assembly is shown in Figure 3.4.

### 3.3 Particle Image Velocimetry (PIV) Measurements

In order to obtain the velocity field over the area of interest, Particle Image Velocimetry (PIV) experiments were conducted for the determined experimental test matrix. Particle Image Velocimetry is a non-intrusive, instantaneous velocity measurement technique, which requires seeding particles that can be visible upstream of the area to be analyzed. The fluid with particles is illuminated with a laser sheet during the measurements. In PIV, the time step is determined by the pulsing frequency of the laser source. Images of the illuminated region with tracer particles are divided into interrogation areas. The first image (frame 1) of the illuminated region at a certain time $t_1$ and the second (frame 2) at time $t_2$ are determined. The illustration of interrogation areas and frames are shown in Fig

3.5. The velocity of the flow in the region is calculated within the knowledge of particle displacement $\Delta x$ and the time difference between first and second pulse $\Delta t$ as given below.

$$U = \frac{\Delta x}{\Delta t} \tag{3.2}$$

In order to obtain the 2-D map of the "instantaneous" velocity field, the velocity in each region is calculated at the time of the recording. PIV also provides extraction of physical information such as streamline topology, vorticity field, Reynolds stress and turbulence stress from the obtained velocity vector map.

TSI 2D Dynamic PIV system was used for the experiments in the study. The basic configuration of a PIV system is composed of:

- Tracer particles
- A double pulse laser with an optical arrangement (a spherical lens and cylindrical lens combination).
- A digital CMOS camera
- A frame grabber
- A synchronizer
- A computer with a Software.

The basic working principle of an ordinary PIV system is illustrated in Figure 3.6.

Seeding tracer particles into the flow plays an important role in velocity measurements. Flow properties and laser capacity are important parameters to choose the appropriate tracer particles used in PIV technique to obtain accurate results. The tracer materials must be large enough to reflect the light from the laser during the imaging process, however at the same time they must be small enough to follow the fluid. Besides that, they must be non-toxic, clean, and

chemically inactive for the health. According to consideration of all those parameters, ViCount Compact 1300 oil based smoke generator aimed for wind tunnel applications were used in this study with a glycol based fog fluid.

The laser system of the PIV is used for illuminating the flow field region. The light scattered by tracer particles travelling in the flow field is recorded by a camera. The displacement of the particles is obtained by capturing the beginning and the final positions of the tracer particles. Litron Nano L 200-15 PIV laser system comprising double pulsed and Q-switched Nd: YAG laser with a visible $532$ nm laser light was used.

The output energy of the laser at $532$ nm was $200$ mJ and repetition rate per laser head ranged between 0-15 Hz. A laser sheet was created by using a set of spherical and cylindrical lenses. For the velocity measurement, the laser was used in the cross flow plane at the dimensionless chordwise distance of $x/C = 0.6$.

Images of the seed particles in the flow field were recorded by a digital TSI Powerview™ Plus 4-megapixel, CMOS camera having $2048 \times 2048$ pixel resolution and equipped with a Nikon $50$ mm F1.8 lens to maintain the flow domain. In this study, $200$ image pairs were taken for each of the investigated cases. The images taken by the camera are read by a frame grabber in the computer. In addition, the frame grabber stores the images as a digital image in the RAM of the computer.

The synchronizer used in the PIV system provides accurate synchronization of system components that includes communication and connection of illumination system and the camera. The time sequenced image of the flow region is captured with the convenient pulse delay by the synchronization of the synchronizer. Insight 4G software was used to control the PIV setup. The separation time ($\Delta t$) between two laser pulses was adjusted corresponding to freestream velocity. During the setting of the separation time for the measurements, the laser sheet

thickness has to be considered in order to ensure the existence of tracer particles inside the illuminated region. The images were captured, after all the settings corresponding to camera, laser and software had been completed. FFT (Fast Fourier Transform) correlation technique was performed as a step of image processing to determine the movement of seeding particles in PIV technique. The images of first and second frame with an interrogation area were analyzed to obtain the average displacement vector. Cross-correlation was the method used in the study to analyze the displacement of the seeding particles over time between the exposure of the first and second frame. In each frame, the interrogation areas were cross-correlated pixel by pixel, with each other. For the common particle movement, the correlation analysis provided the location of highest correlation peak. The velocity and the measurement of the movement was obtained with sub-pixel interpolation. Repeating the cross-correlation process for each interrogation area over the two image frames provided to obtain a velocity vector map for the whole target area. After correlation procedure, Tecplot was used to observe the streamlines, velocity magnitude, and vorticity results.

The schematic representation of the PIV setup with the connections among the components is shown in Figure 3.7. The laser sheet was located perpendicular to the freestream at the obtained dimensionless chordwise distance of $x/C = 0.6$. In addition, the PIV camera was adjusted perpendicular to the vertical side of the tunnel which was located outside the test section. As shown in figure, a rectangular mirror with a dimension of $15 \times 25$ cm was located inside the test section at nine chord distance downstream of the wing with an orientation angle of $45°$ to the freestream in order to capture the flow field.

### 3.4 Flow control set-up

The flow control set-up includes four components, which are thermocouples, data logger, resistance wire heater, and DC power supply. The schematically

representation of the control test-setup is shown in Figure 3.8.

Type T thermocouples, indicating linear relation within the measurement range of $-200$ to $350℃$, were used in this study in order to measure the temperature on the suction side of the wing. Fifteen thermocouples wires, each $1200$ mm in length were used and positioned into the wing through holes, which were drilled $2$ mm in diameter. Only half surface of the wing was used for positioning the thermocouples due to the fact that the flow structure over the wing was symmetric which was confirmed with the preliminary experiments conducted. The distribution of the thermocouples on the wing is illustrated in Figure 3.9.

Temperature measurements were recorded using an Agilent Data Logger which had $20$ channels. The data logger device was connected to a laptop PC and the temperature readings were monitored through the BenchLink Data Logger 3 software at 1 Hz for about an hour in order to reach steady-state condition. The program had self-calibration option for the respective thermocouple type.

A custom designed resistance wire heater was used to heat the wing model. It was located on the pressure side of the wing in order to perform the velocity measurement on the suction side. The heater was produced such that the resistance wire was coiled up with a $10$ mm step around a mica sheet that had equal dimensions with the pressure side of the planform. The resistance wire is $0.4$ mm in diameter and made of $Cr_{23}Al_5$ which can resist up to $10.95\ \Omega$. In addition, the coiled mica sheet was covered with a proper heat resistive shield. A mica sheet was placed between thermocouples and resistance wire heater in order to prevent the direct contact. The gap between the leading edge of the wing and

the heater was filled by thermal paste to provide a smooth leading edge surface. Obtaining a uniform heat flux was aimed in the study. The positioned resistance wire heater on pressure side of the wing is shown in Figure 3.10.

The required operating voltage for the heating system was supplied from DC power supply. A maximum of 60 V voltage can be reached by running the device in series mode. The amount of the heat rate supplied by the heater to the wing can be controlled by adjusting the operating voltage of the DC power supply.

In this study, the heating conditions were quantified by taking the approximate temperature difference ($\Delta T$) between the ambient temperature ($T_\infty$) and the temperature of the heated wing surface ($T_s$) into account. Two sets of experiments were performed separately, during steady-state condition and during the transient period. For the steady-state experiments, three different heat flux sets were provided on the wing model; low, medium, and high, according to the corresponding power input values and the resulting temperature differences. Low heat flux sets corresponds to $15 \leq \Delta T \leq 25$ when medium heat flux sets corresponds to $25 \leq \Delta T \leq 35$. In addition, medium heat flux sets changes between $35 \leq \Delta T \leq 45$. The velocity measurements were performed once the steady-state condition was achieved according to temperature measurements, which means that all the readings from thermocouples were stabilized and converged to a value over a period of time. Figure 3.11 shows the temperature variation from the initiation of power input until steady-state conditions, for the low heat flux case at $Re = 8000$ and $\alpha = 4°$ for representative purposes. In order to observe the flow over the wing during the transient period until steady-state condition, simultaneous velocity measurements were performed. Investigation of the velocity field with PIV measurements were conducted separately at eight different surface temperature values for the high heat flux condition at $Re = 3000$ and $\alpha = 10°$ and at seven different surface temperature values for the low heat

flux condition at $Re = 8000$ and $\alpha = 7°$. For the high heat flux case, the variation of temperature as a function of time and eight different surface temperature values corresponding to PIV measurements at $Re = 3000$ and $\alpha = 10°$ is plotted in Figure 3.12.

### 3.4.1 Experimental matrix

In this study, the experimental matrix was prepared for steady-state heating condition and for the transient period experiments only two cases were selected from among total of 52 experiments. The experiments were performed at four different attack angles; $\alpha = 4°, 7°, 10°$ and 13° for $Re = 3000$, $Re = 8000$ and $Re = 10000$. $Re = 2000$ at $\alpha = 4°$ were also performed as representative case in order to understand the effect of heating in high Reynolds number. Figure 3.13 shows the experimental matrix of the current study for steady-state heating condition. In addition, the difference in temperature $\Delta T[K]$ between the heated wing surface $T_s$ and the ambient temperature $T_{\infty}$. corresponding for each case is provided in Table 3.1. Two additional cases were also selected in order to investigate the flow during the transient period. As mentioned above, the measurements of PIV were performed at $Re = 3000$ for $\alpha = 10°$ and for $Re = 8000$ at $\alpha = 7°$ for the transient period.

Table 3.1 Experimental matrix for the steady-state heating condition

| Angle of attack | Reynolds Number | Low heat flux $\Delta T\ (K)$ | Medium heat flux $\Delta T\ (K)$ | High heat flux $\Delta T\ (K)$ |
|---|---|---|---|---|
| $\alpha = 4^{\circ}$ | 3000 | 16 | 27 | 36 |
| | 8000 | 20 | 30 | 40 |
| | 10000 | 18 | 28 | 37 |
| | 20000 | 27 | 35 | 44 |
| $\alpha = 7^{\circ}$ | 3000 | 17 | 27 | 37 |
| | 8000 | 21 | 32 | 42 |
| | 10000 | 21 | 30 | 40 |
| $\alpha = 10^{\circ}$ | 3000 | 18 | 28 | 39 |
| | 8000 | 23 | 32 | 42 |
| | 10000 | 22 | 32 | 43 |
| $\alpha = 13^{\circ}$ | 3000 | 19 | 29 | 39 |
| | 8000 | 24 | 34 | 43 |
| | 10000 | 23 | 33 | 43 |

### 3.5 Uncertainty Estimates

In an experimental study, the accuracy of the data is critical. The data must be validated before analysis or design. Uncertainty analysis is the procedure to apply in order to check the accuracy of the data.

During the experimental measurements, two different types of errors exist: systematic (or fixed) error and random error (nonrepeatability). Correction or calibration methods can be used to remove the systematic error. However, potential random error in the results can only be reduced by uncertainty analysis.

In this study, possible sources of uncertainties accounted in calculation of heat transfer coefficient and velocity measurements of Particle Image Velocimetry are tried to be documented.

The calculation of the estimate uncertainty of a result R which is a function of n number of measured values is formulated in the following Equation 3.3 [83].

$$\omega_R = \left[\left(\omega_{x_1}\frac{\partial R}{\partial x_1}\right)^2 + \left(\omega_{x_2}\frac{\partial R}{\partial x_2}\right)^2 + \cdots + \left(\omega_{x_n}\frac{\partial R}{\partial x_n}\right)^2\right]^{1/2} \tag{3.3}$$

The uncertainty estimate of the each measured values is represented as $\omega_{x_i}$. In addition, the relative uncertainty of each measured values can be calculated as in Equation 3.4.

$$\frac{\omega_R}{R} = u_R \tag{3.4}$$

Convective heat transfer coefficient can be calculated with the knowledge of heat flux and the difference in temperature $\Delta T\ [K]$ between the heated wing surface $T_s$ and the ambient temperature $T_\infty$. Heat flux is the function of the electrical power input including the multiplication of voltage, *V*, in volts and electric current, *I*, in amperes per unit heat transfer area of the wing surface. The following Equation 3.5 shows the calculation of convective heat transfer coefficient (detailed information in Chapter 4) from the above mentioned variables,

$$h = \frac{V \cdot I}{A \cdot (T_s - T_\infty)} \tag{3.5}$$

Taking the Equation 3.5 into account, the uncertainty propagation for convective heat transfer coefficient is calculated using the Equation 3.3, would give the uncertainty of convective heat transfer coefficient as follows,

$$\omega_h = \left[\left(\omega_V \frac{\partial h}{\partial V}\right)^2 + \left(\omega_I \frac{\partial h}{\partial I}\right)^2 + \left(\omega_A \frac{\partial h}{\partial A}\right)^2 + \left(\omega_{T_s} \frac{\partial h}{\partial T_s}\right)^2 + \left(\omega_{T_\infty} \frac{\partial h}{\partial T_\infty}\right)^2\right]^{1/2} \tag{3.6}$$

$\omega_{x_i}$ values are embedded into Equation 3.3 depending upon the respective uncertainty values of each measurand. The measurement accuracy of the electrical power includes voltage value of 0.1V and ampere value of 0.01A. The accuracy of the wing area depends on the resolution of the ruler which corresponds to 0.1 mm. In addition, measurements of surface and ambient

temperature is performed with an accuracy of the Data Logger $\mp 1$℃. From above conclusions the relative uncertainty value is found as 8.5 % for the maximum heat transfer coefficient value and as 3.6 % for the minimum one.

Apart from the uncertainties obtained from calculation of convective heat transfer coefficient, there was a critical issue that induced a limitation while forming the experimental matrix. Tracer particles began to have an entrainment problem in the flow field with increasing heat input rate. Thus, in low Reynolds number flows, the heat input rate had a maximum limit in order for tracer particles to be entrained into the flow field. Nonhomogeneous flow distribution was obtained in the field of interest due to this problem. As a result of the entrainment problem, different ranges of uncertainty values were obtained from PIV measurements. To determine the uncertainty of PIV measurements, the Peak Ratio (PR) uncertainty method is used by Insight software. This method uses the Peak to noise Peak Ratio to determine the uncertainty. Many possible sources of error (e.g., particle seeding density, pixel displacement, image pre-processing, etc.), are incorporated in the PR method. The PR method determines uncertainties for two-dimensional PIV. Insight software calculates two-dimensional velocity vectors in the PIV application. Three different sample cases were used to clarify the uncertainty calculation. First, the case at $Re = 8000,\ \alpha = 7°$ for no heat input condition was selected to understand the heating effect. The low heat flux condition for $Re = 8000$ at $\alpha = 7°$ was used in order to obtain homogeneous flow distribution. Finally, at $Re = 8000$ for $\alpha = 10°$, nonhomogeneous flow distribution was obtained to determine the maximum uncertainty of PIV measurements. The comparison of the representative raw images, velocity magnitudes and uncertainty results for three sample cases is presented in Figure 3.14. According to comparisons of three representative cases for uncertainty analysis of PIV, the magnitude of the velocities was obtained similar for each cases. The results of uncertainty of PIV shows that, low level and homogenous uncertainty was

obtained in the field of interest for zero and low heat flux cases. By increasing heat, the maximum uncertainty results were obtained for the highest heat flux condition for $Re = 8000$ at $\alpha = 10°$ that represented nonhomogeneous flow field near the wing surface.

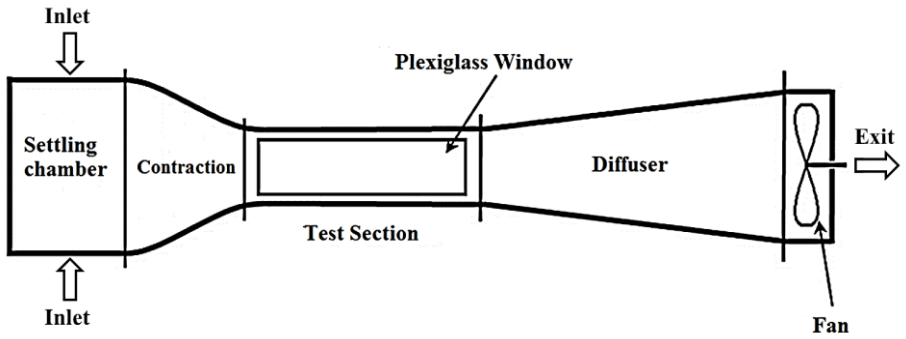


Figure 3.1 Schematic view of wind tunnel

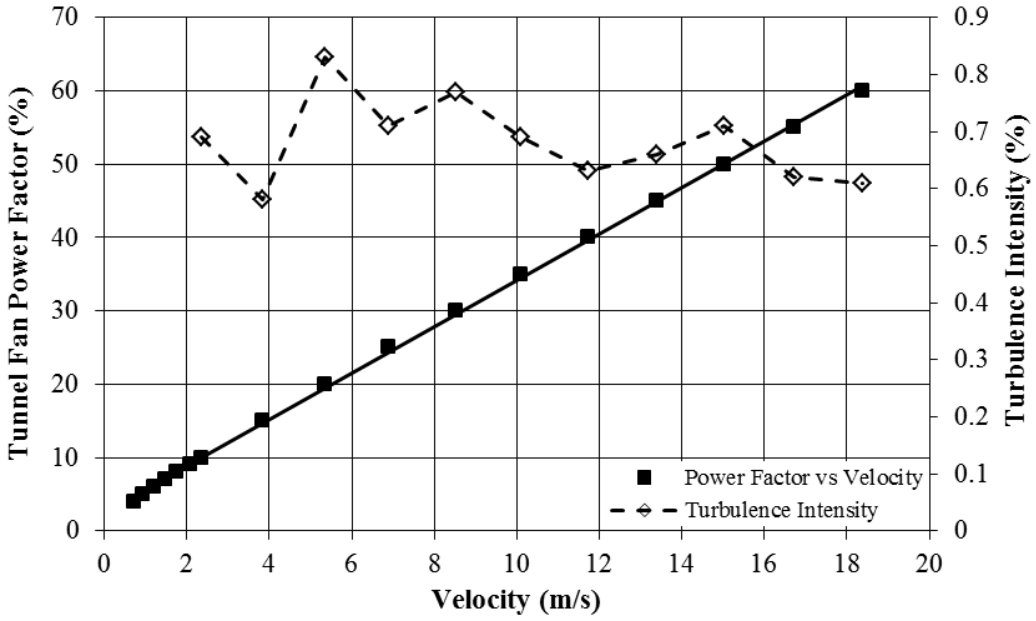


Figure 3.2 Wind tunnel calibration graph

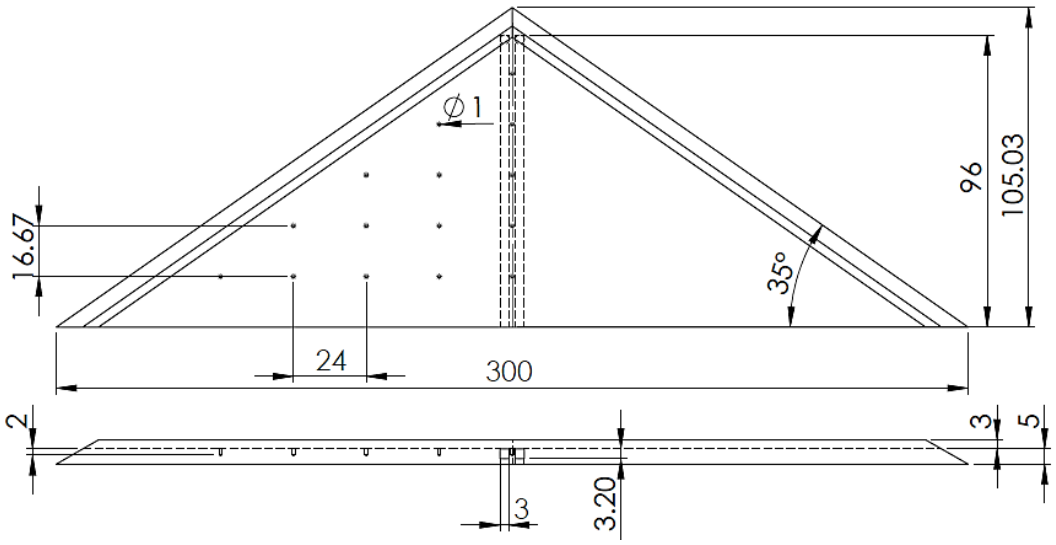


Figure 3.3 CAD drawing of the designed wing

Figure 3.4 The views of wing, mount and test section assembly

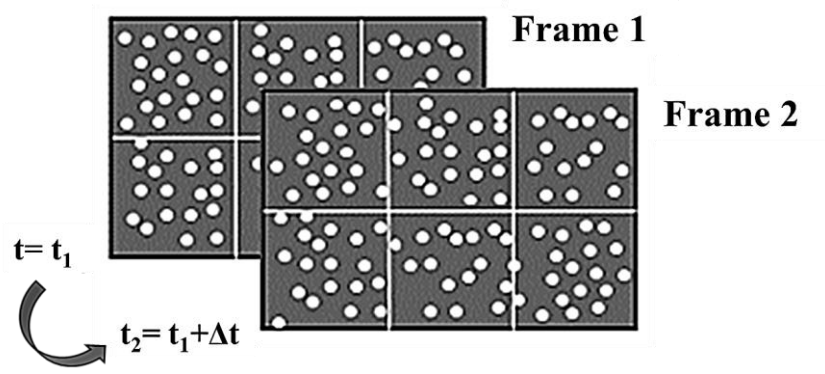


Figure 3.5 Interrogation areas in first and second frame

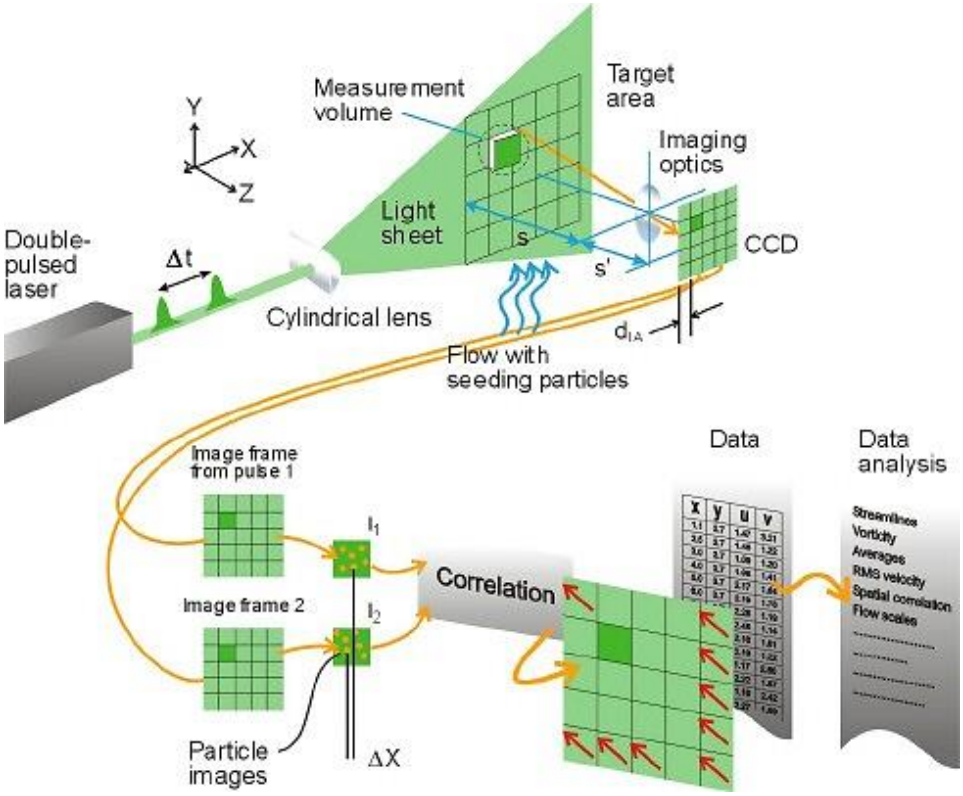


Figure 3.6 Working principle of Particle Image Velocimetry (PIV) system [84]

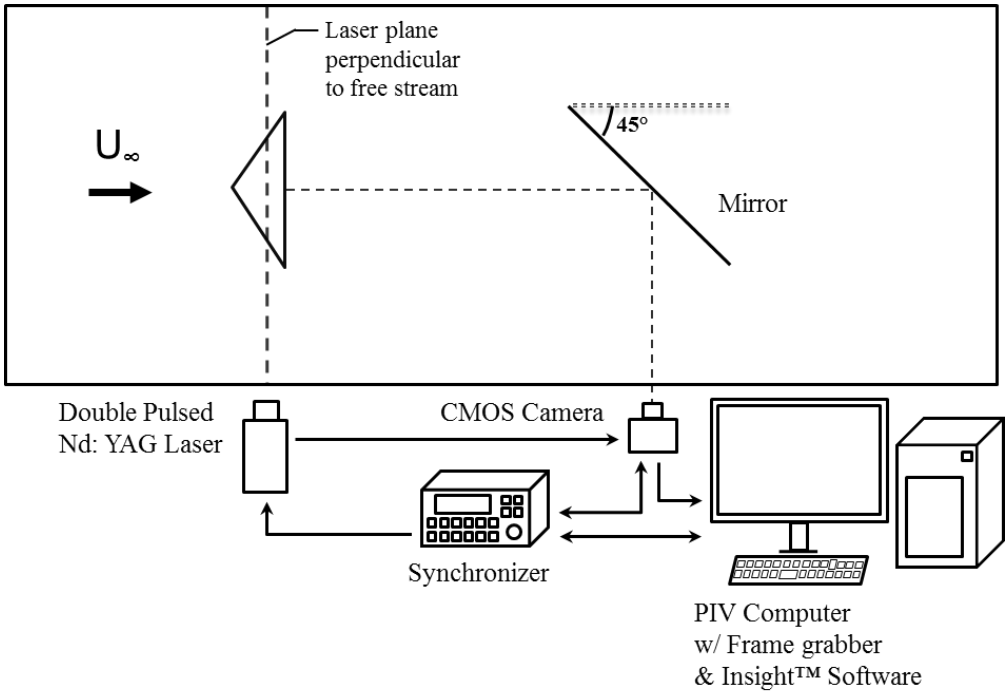


Figure 3.7 The schematic view of the PIV setup and the connections among the components of PIV

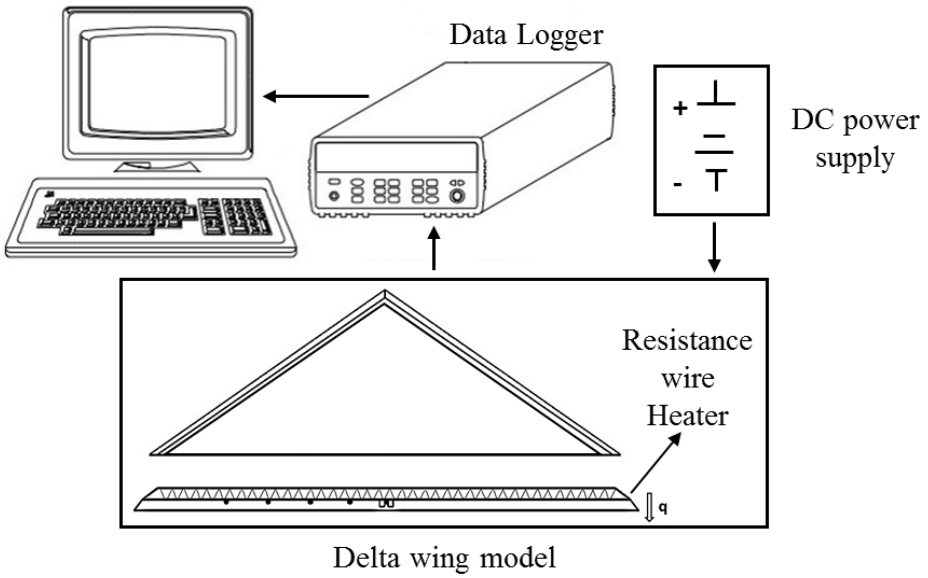


Figure 3.8 The schematic view of control setup

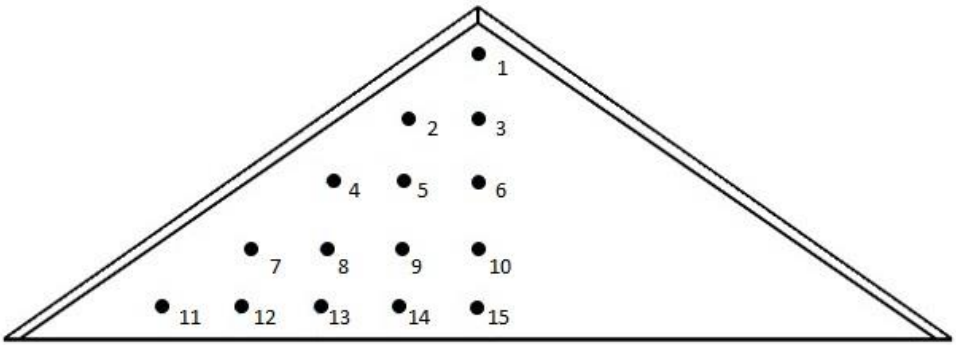


Figure 3.9 Location of thermocouples on the left side of the wing

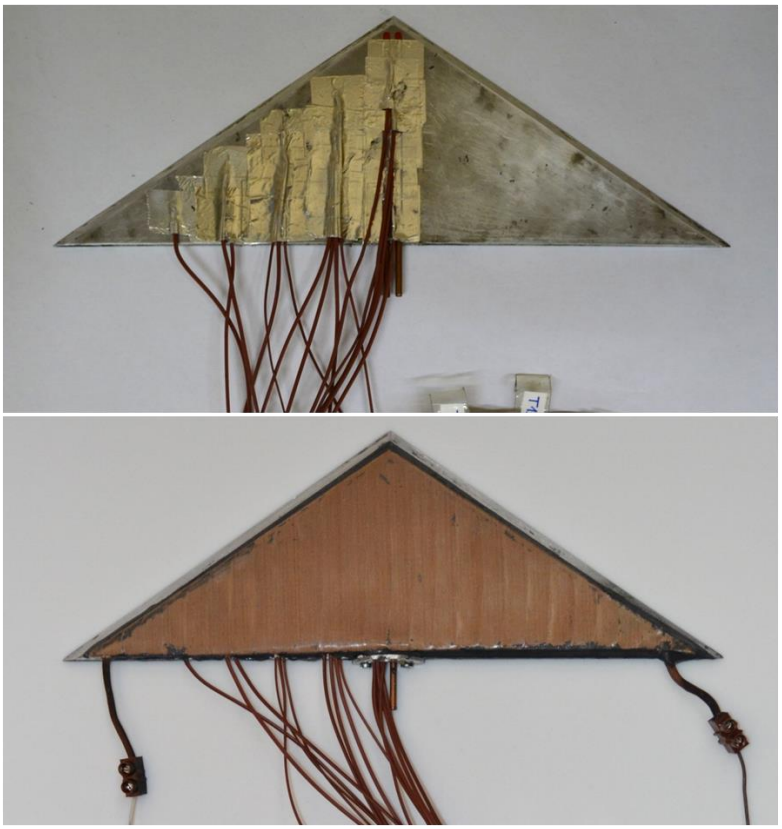

Figure 3.10 Fabricated wing for control set-up with resistance wire heater and thermocouples

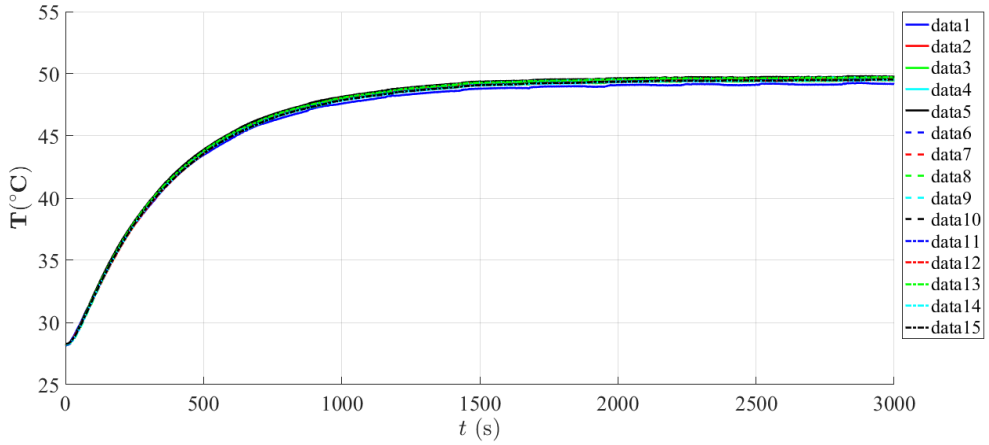


Figure 3.11 The temperature variation from the initiation of wing heating until steady-state condition at $Re = 8000$ and $\alpha = 4°$

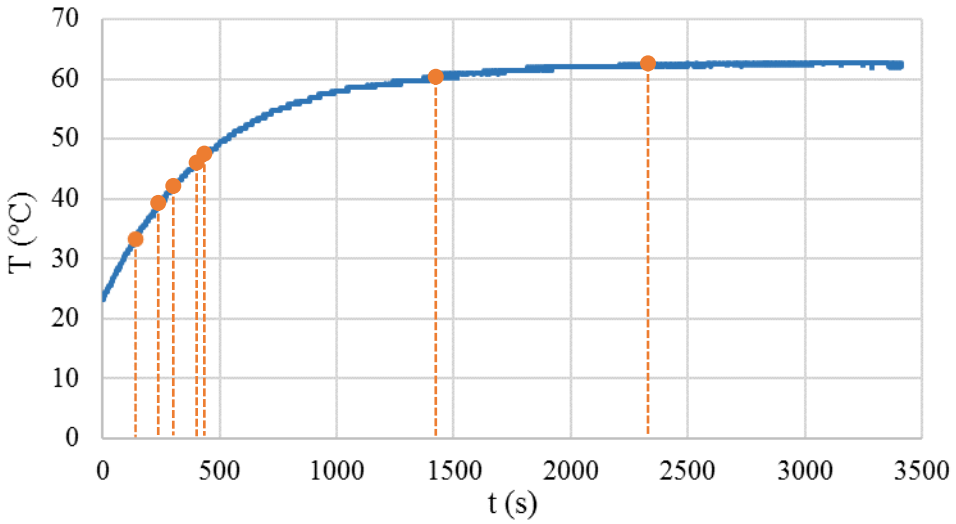


Figure 3.12 The temperature variation during the transient period at $Re = 3000$ and $\alpha = 10°$ with the measured temperature values for PIV measurements

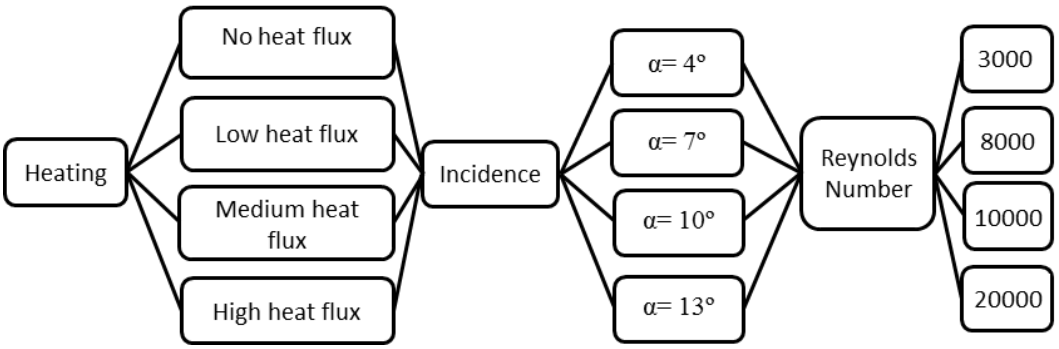


Figure 3.13 Experimental matrix for steady-state heating

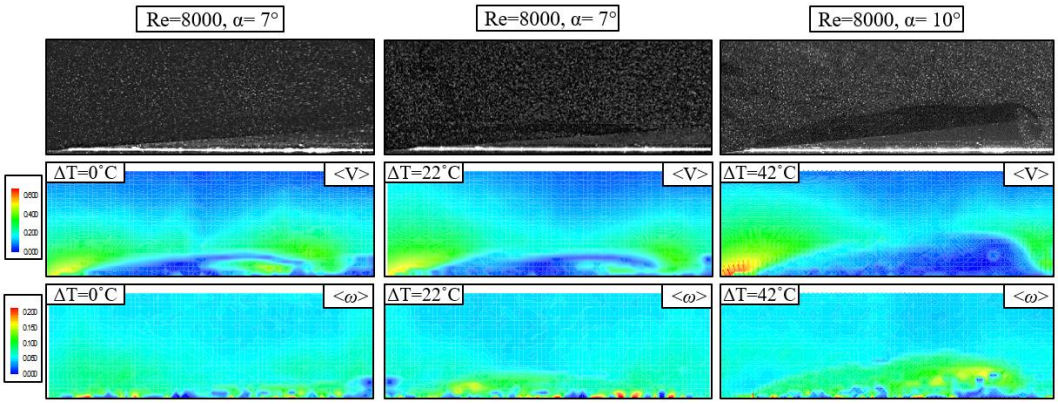


(a) (b) (c)

Figure 3.14 Comparison of (a) zero heat flux condition at $Re = 8000$ and $\propto = 7°$, (b) low heat flux condition at $Re = 8000$ and $\propto = 7°$, and (c) high heat flux condition at $Re = 8000$ and $\propto = 10°$ for raw images (top row), velocity magnitude (second row), and standard uncertainty value(bottom row)

# CHAPTER 4

# RESULTS AND DISCUSSION

In this chapter, the results of the experiments conducted are given and discussed in detail. The chapter is divided into three parts. First, the PIV measurements employed for steady-state conditions are reported. Then, the velocity measurements for transient period are presented. For both cases; streamlines ($\psi$), the time-averaged velocity vectors ($\boldsymbol{V}$) and the contours of constant non-dimensional axial vorticity ($\omega C/U_\infty$) are plotted. Finally, calculations and discussions about temperature measurements are presented in two sections; data reduction and plots of temperature calculations.

## 4.1 Particle Image Velocimetry measurement results for steady-state heating condition

Effect of the steady state heating on the flow structure of a low swept delta wing was investigated via crossflow PIV. The velocity measurements were performed at the chordwise distance of $x/C = 0.6$ for all cases. Preliminary tests were performed to check the symmetry in the flow field. Once this was confirmed, half of the wing was used in PIV experiments.

Figures 4.1 to 4.12 show velocity measurement results for four different attack angles $\alpha = 4°, 7°, 10°$ and $13°$ at three different Reynolds numbers of $3000, 8000$ and $10000$ respectively. Each figure is constructed in the same format such that; columns show streamlines ($\psi$), the time-averaged velocity vectors ($\boldsymbol{V}$) and the contours of constant non-dimensional axial vorticity ($\omega C/U_\infty$) and the rows represent the no heat flux, low, medium and high heat flux conditions respectively.

Considering the results for $Re = 3000$ and $\alpha = 4°$ represented in Figure 4.1, a leading edge vortex pattern is apparent in the structures of all cases. It is evident from the streamlines and the velocity vectors, that the location of the vortex core slightly moves towards the inboard of the symmetry plane from no heat flux case to high heat flux case. In addition, the level of the vorticity contours decreases by increasing heat flux. Magnitude of the velocity vectors also decreases from zero to high heat flux case. In addition, the core of the vortical structure starts to diminish on the high heat flux case according to the streamtraces.

Figure 4.2 shows the results at $Re = 3000$ and $\alpha = 7°$. Increasing the attack angle to $\alpha = 7°$ leads to the formation of stronger vortex structure compared to the $\alpha = 4°$ case. Amplification of the heat flux deteriorates the flow field considerably. According to the streamlines, the velocity vectors and vorticity contours, and the reattachment location significantly shifts towards the symmetry plane with increase in heat flux and in addition the magnitude of the velocity vectors also decreases. The distribution of the vorticity contours broadens in a scattered manner while the level decreases with the increasing heat input.

The results of the velocity measurements for $Re = 3000$ at $\alpha = 10°$ are shown in Figure 4.3. The effects are different from the results represented for the attack angle $\alpha = 4°$ and $\alpha = 7°$. In no heat flux and all heat flux inputs, the velocity vectors show that the rotational core is very close to the centerline of the wing where the shear layers reattach to the wing surface. This can be the trace of pre-stall condition. According to the vorticity contours, the scattered flow structure in no heat flux condition is recovered with increasing heat flux. In addition, the spatial extent and the level of the vorticity increases in the vicinity of the rotational core with increasing heat flux. Elongated shear layers from the leading edge of the wing were also observed. The velocity vector and the vorticity contours show that, the location of the vortex core slightly moves towards the

leading edge by increasing heat flux as well.

Figure 4.4 shows the results at $Re = 3000$ and $\alpha = 13°$. By increasing the attack angle to $\alpha = 13°$, shear layers are directly merged to the symmetry plane of the wing, which could be a clear indication of stall condition compared to the $\alpha = 10°$.

When the attack angle reaches $\alpha = 13°$, the symmetrical flow structure isn't observed in the flow field. The flow is shifted from the symmetry plane with increasing heat input. According to the vorticity contours, the level of the contours increases as the heating increases. In addition, the scattered flow field merged and elongated flow structure occurs.

Figure 4.5 shows the results for $Re = 8000$ at $\alpha = 4°$. There is no considerable effect of heating in streamlines and vector field compared to the results in Figure 4.1. Although the spatial extent of the vortical structure does not change, the level of the vorticity contours also decreases especially in the vicinity of the vortex cores with increasing heat flux added to the flow field.

The results for $Re = 8000$ at $\alpha = 7°$ are shown in Figure 4.6. Here, similar flow patterns and observations as those for $Re = 3000$ and $\alpha = 7°$ (see Figure 4.2) are valid. The velocity vectors show that the magnitude of the velocity vectors in the vicinity of the vortex core decreases from no heat flux to low heat flux case. According to the velocity vectors and vorticity contours, the location of the vortex core slightly moves towards the inboard of the centerline with increasing heat input from no heat flux case to the low heat flux condition. However, the movement is not so evident between other heat flux conditions. The vorticity contours show that the level of the vorticity decreases with increasing heat flux.

Figure 4.7 demonstrates the results of the velocity measurements for $Re = 8000$ at $\alpha = 10°$. Pre-stall condition is apparent from streamlines and vorticity

contours for no heat flux and all heat flux conditions by increasing the angle of attack from $\alpha = 7°$ to $\alpha = 10°$. The velocity vectors and the vorticity contours represent that the location of the vortex core slightly moves towards the leading edge. In addition, the vorticity level increases from no heat flux to high heat flux condition.

The results of the velocity measurements for $Re = 8000$ at $\alpha = 13°$ are shown in Figure 4.8. A similar flow pattern as for $Re = 3000$ at $\alpha = 13°$ (see Figure 4.4) is observed. According to the vorticity contours, small scale discrete vortical structures are demonstrated near the surface of the wing due to the entrainment problem of tracer particles with increasing attack angle. There is no apparent difference from no heat flux case to high heat flux condition.

The results of the velocity measurements for $Re = 10000$ at $\alpha = 4°$ are shown in Figure 4.9. Dual leading edge vortex structure is apparent from streamlines and vorticity contours for no heat flux and all heat flux cases. The structure of the field does not considerably change across the respective cases. The concentration of the vorticity contours decreases in low and medium heat flux conditions compared to the no heat flux case. However, the high heat flux case exhibits more condensed contours in the vortex core close to the centerline compared to the all other cases in this figure. In addition to very slight movement of the reattachment line towards the wing inboard, the secondary vortex that splits primary vortex is evident with condensed contours in high heat flux condition.

Figure 4.10 shows the results at $Re = 10000$ and $\alpha = 7°$. According to streamlines and vorticity contours, dual vortex structure is also apparent for the heating cases except the high heat flux case. Even though there is no significant change in velocity vectors and the level of the vorticity, the spatial extent of the structures increases by increasing heat flux.

Figure 4.11 represents the results for $Re = 10000$ at $\alpha = 10°$. Similar flow patterns and observations are valid for $Re = 3000$ and $Re = 8000$ at the same angle of attack α= 10º. The vorticity contours show that the vortex core slightly moves towards the leading edge when the heating input increases. In addition, the vorticity levels increase in the vicinity of the vortex core.

The results of the measurements at $Re = 10000$ for $\alpha = 13°$ are shown in Figure 4.12. Stall condition is apparent for no heat flux and all heat flux cases according to the velocity vectors and vorticity contours.

The results of the velocity measurements for $Re = 20000$ at $\alpha = 4°$ are presented in Figure 4.13. $Re = 20000$ at $\alpha = 4°$ is selected as a representative case to investigate the higher Reynolds number. Dual vortex structure is apparent from streamlines and vorticity contours for no heat flux and all heat flux cases. The velocity vectors show that, the vortex core location that is close to the centerline slightly moves towards the wing inboard with increasing heat input from no heat flux case to the high heat flux condition. This is also evident from streamlines. In addition, the magnitude of the velocity vectors in the vicinity of the vortex core close to the symmetry plane decreases from no heat flux to high heat flux case.

### 4.2 Particle Image Velocimetry measurement results for the transient period

The results of the velocity measurements for $Re = 3000$ at $\alpha = 10°$ are shown in Figure 4.14. The time-averaged streamline patterns, velocity vectors and non-dimensional vorticity contours for transient period are presented for no heat flux and all heat flux conditions. Pre-stall condition is apparent for steady-state heating cases shown in the previous section. The beginning case (first row in Figure 4.14) that corresponds to no heat flux and the final case (last row in Figure 4.14) which coincides with the high heat flux condition at $Re = 3000$ and $\alpha = 10°$ are identical to steady-state heating conditions. For the transient period input, pre-stall

condition can also be seen for all cases. The velocity vectors and the vorticity contours show that, the location of the vortex core slightly moves toward the leading edge as the heat input increases and this case is also evident from the streamline patterns. According to the vorticity contours, the level of the vorticity increases by increase in heat input, especially proximity of the wing surface. The spatial extent of the vorticity also increases with increasing heat input. In addition, elongated shear layers from the leading edge of the wing were also obtained.

Figure 4.15 shows the results for second transient period at $Re = 8000$ and $\alpha = 7°$. The velocity vectors demonstrate that, the magnitude of the velocity vectors in the vicinity of the vortex core decreases from no heat flux to low heat flux case as stated in steady-state heating condition. Slight displacement of the vortex core toward the centerline of the wing is seen from the velocity vectors and vorticity contours with increasing heat from no heat flux case to the high heat flux condition. According to the vorticity contours, the level of the vorticity decreases with increasing heat flux.

### 4.3 Temperature measurements for steady-state heating condition

The results of temperature measurements taken from fifteen thermocouples positioned in the delta wing (see Figure 3.19) are presented and discussed in detail. The calculations and discussions about plotted results are presented for the experimental matrix used in the steady state heating condition. The formulations of the calculations are given under the data reduction section and the plots are presented in the last section of this chapter.

#### 4.3.1 Data reduction

The results of temperature measurements from fifteen thermocouples are used to calculate two parameters; convection heat transfer coefficient $h$ $[W/m^2K]$ and

Nusselt number, $Nu$. The amount of heat transferred per unit surface area, also known as heat flux, $q"$ $[W/m^2]$, is calculated using the electrical power input per unit heat transfer area of the wing surface. Electrical power is the product of voltage, *V*, in volts and electric current, *I*, in amperes using data taken from the DC power supply.

$$q" = \frac{V \cdot I}{A} \tag{4.1}$$

Convective heat transfer coefficient can be calculated with the knowledge of heat flux and the difference in temperature $\Delta T$ $[K]$ between the heated wing surface $T_s$ and the ambient temperature $T_\infty$, as provided below.

$$h = \frac{q"}{\Delta T} \tag{4.2}$$

Nusselt number is a non-dimensional parameter that can be inferred as the ratio of total convective heat transfer to conductive heat transfer across the solid-fluid boundary.

$$Nu = \frac{h \cdot C}{k} \tag{4.3}$$

Here, $C$ $[m]$ is the chord length, used as the characteristic length of the wing. The thermal conductivity of the fluid $k$ $[W/mK]$ is obtained separately for each case according to the film temperature $T_f$ defined below.

$$T_f = \frac{T_s + T_\infty}{2} \tag{4.4}$$

The results of the convective heat transfer coefficient and Nusselt number calculations are tabulated in Table 4.1. In addition, a sample calculation is provided in Appendix B.

Table 4.1 Convective heat transfer coefficient and Nusselt number values for the steady-state condition for the experimental matrix

| α= 4° | Heat flux | q ($W/m^2$) | ΔT (K) | h ($W/m^2K$) | Nu |
|---|---|---|---|---|---|
| Re=3000 | Low | 774,60 | 17,00 | 45,56 | 177,20 |
| | Medium | 1206,35 | 26,00 | 46,40 | 178,45 |
| | High | 1752,38 | 37,00 | 47,36 | 178,88 |
| Re=8000 | Low | 1206,35 | 21,00 | 57,45 | 223,40 |
| | Medium | 1752,38 | 30,00 | 58,41 | 224,66 |
| | High | 2377,78 | 40,00 | 59,44 | 225,33 |
| Re=10000 | Low | 1206,35 | 20,00 | 60,32 | 236,32 |
| | Medium | 1752,38 | 28,00 | 62,59 | 242,49 |
| | High | 2377,78 | 37,00 | 64,26 | 245,37 |
| Re=20000 | Low | 2377,78 | 27,00 | 88,07 | 339,96 |
| | Medium | 3098,41 | 35,00 | 88,53 | 340,48 |
| | High | 3971,43 | 44,00 | 90,26 | 342,14 |

| α= 7° | Heat flux | q ($W/m^2$) | ΔT (K) | h ($W/m^2K$) | Nu |
|---|---|---|---|---|---|
| Re=3000 | Low | 774,60 | 18,00 | 43,03 | 169,23 |
| | Medium | 1206,35 | 27,00 | 44,68 | 172,48 |
| | High | 1752,38 | 38,00 | 46,12 | 175,44 |
| Re=8000 | Low | 1206,35 | 22,00 | 54,83 | 213,24 |
| | Medium | 1752,38 | 31,00 | 56,53 | 217,42 |
| | High | 2377,78 | 41,00 | 57,99 | 219,84 |
| Re=10000 | Low | 1206,35 | 21,00 | 57,45 | 223,40 |
| | Medium | 1752,38 | 30,00 | 58,41 | 225,49 |
| | High | 2377,78 | 40,00 | 59,44 | 226,15 |

| α= 10° | Heat flux | q ($W/m^2$) | ΔT (K) | h ($W/m^2K$) | Nu |
|---|---|---|---|---|---|
| Re=3000 | Low | 774,60 | 19,00 | 40,77 | 158,54 |
| | Medium | 1206,35 | 28,00 | 43,08 | 165,10 |
| | High | 1752,38 | 39,00 | 44,93 | 170,32 |
| Re=8000 | Low | 1206,35 | 23,00 | 52,45 | 203,22 |
| | Medium | 1752,38 | 32,00 | 54,76 | 209,09 |
| | High | 2377,78 | 42,00 | 56,61 | 213,83 |
| Re=10000 | Low | 1206,35 | 22,00 | 54,83 | 215,24 |
| | Medium | 1752,38 | 31,00 | 56,53 | 219,83 |
| | High | 2377,78 | 41,00 | 57,99 | 221,43 |

Table 4.2 continued

| α= 13° | Heat flux | q (W/m$^2$) | ΔT (K) | h (W/m$^2$K) | Nu |
|---|---|---|---|---|---|
| Re=3000 | Low | 774,60 | 19,00 | 40,77 | 159,73 |
| | Medium | 1206,35 | 29,00 | 41,60 | 159,99 |
| | High | 1752,38 | 39,00 | 44,93 | 170,32 |
| Re=8000 | Low | 1206,35 | 24,00 | 50,26 | 196,93 |
| | Medium | 1752,38 | 34,00 | 51,54 | 198,96 |
| | High | 2377,78 | 44,00 | 54,04 | 204,85 |
| Re=10000 | Low | 1206,35 | 23,00 | 52,45 | 207,04 |
| | Medium | 1752,38 | 32,00 | 54,76 | 212,18 |
| | High | 2377,78 | 43,00 | 55,30 | 210,75 |

### 4.3.2 Plots of temperature calculations

In this section, three different kinds of plots are provided. First, the relation between Nusselt number and Reynolds number at each angle of attack is presented in Figures 4.16-4.19. Later, for each heat flux condition (low, medium and high), the relation between Nusselt number and Reynolds Number are shown in Figures 4.20-4.22. Finally, the relation between convective heat transfer coefficient and Reynolds number for the whole experimental matrix is given in Figure 4.23. In addition, the relation between Nusselt number and Reynolds number for the whole experimental matrix is also given in Figure 4.24.

The variation of Nusselt number with Reynolds number at $\alpha = 4°$ is shown in Figure 4.16. For all heat flux cases, Nusselt number increases with increasing Reynolds number. In addition, when the heat rate increases for each Reynolds number, Nusselt number also increases slightly in all cases, a result of the direct proportionality between Nusselt number and heat flux. For $Re = 10000$, the change in Nusselt number with increasing heat rate is more than $Re = 3000, Re = 10000$ and $Re = 20000$.

Figure 4.17 demonstrates the Nusselt number and Reynolds number relation at $\alpha = 7°$. The results of plotted data show that Nusselt number increases with increasing heat input. For $Re = 10000$, corresponding Nusselt numbers have less variation among low, medium, and high heat flux conditions. In addition, Nusselt number increases by increasing Reynolds number for all cases.

The relation between Nusselt number and Reynolds number at $\alpha = 10°$ is plotted in Figure 4.18. In line with the attack angles of $\alpha = 4°$ and $\alpha = 7°$, increasing Reynolds number induces an increase in Nusselt number. In addition, Nusselt number increases from no heat flux to high heat flux case for each Reynolds number.

Figure 4.19 shows the result of Nusselt number and Reynolds number relation at $\alpha = 13°$. By increasing Reynolds number, Nusselt number also increases at $Re = 3000$ and $Re = 8000$. However, Nusselt number result for medium heat flux case is higher than high heat flux case due to having an uncertainty of calculation in convective heat transfer coefficient according to temperature measurements.

The results of Nusselt number and Reynolds number relation for low heat flux cases are shown in Figure 4.20. For all Reynolds number values, Nusselt number decreases when the attack angle increases. The maximum Nusselt number results are obtained at $\alpha = 4°$ for each Reynolds number. In addition, Nusselt number increases with increasing Reynolds number for each angle of attack. The maximum Nusselt number values are observed at $Re = 20000$ and the angle of attack $\alpha = 4°$.

The relation between Nusselt number and Reynolds number at $\alpha = 10°$ are plotted for medium heat flux cases in Figure 4.21. Nusselt number reaches its highest value in lowest angle of attack. For each Reynolds number, the highest Nusselt number values are obtained at $\alpha = 4°$. In addition, by increasing Reynolds

number, Nusselt number increases for each angle of attack. Thus, the highest Nusselt number is obtained at the highest Reynolds number $Re = 20000$.

Figure 4.22 presents the Nusselt number and Reynolds number relation for high heat flux cases. Nusselt number decreases with increasing angle of attack. In addition, the results of Nusselt number and Reynolds number relation are also similar to those for low heat flux and medium heat flux cases for each angle of attack. The values of Nusselt number increase with increasing Reynolds number. Thus, the highest Nusselt number values are obtained at the highest Reynolds number and the lowest angle of attack.

Figure 4.23 is the summary of all the results for Nusselt number versus Reynolds number for the whole experimental matrix. For all cases, Nusselt number increases with increasing Reynolds number at each angle of attack. By increasing heat input rate, Nusselt number increases for all angles of attack, except for $Re = 10000$ and $\alpha = 13°$. Nusselt number corresponding to medium heat flux condition is higher than high heat flux condition for $Re = 10000$ and $\alpha = 13°$. In addition, for each Reynolds number, Nusselt number increases with decreasing attack angle.

The results of the relation between convective heat transfer coefficient and Reynolds number is shown for the whole experimental matrix in Figure 4.24. Similar observations are obtained as with the Nusselt number versus Reynolds number plot, since the two variables $Nu$ and $h$ are related through the thermal conductivity of air, which only slightly varies with film temperature and the constant chord length. Thus, convective heat transfer coefficient also increases with increasing Reynolds number for all cases. When the heat rate increases, convective heat transfer coefficient also increases for all cases at each angle of attack. Moreover, convective heat transfer coefficient increases for each Reynolds number by decreasing attack angle.

### 4.4 Discussion on the effect of wing heating on flow structure

The effect of wing heating on flow structure was investigated by applying uniform heat flux on the pressure side of the wing. The wing was positioned into the wind tunnel such that the suction side was kept as the top surface where the air movement associated with the buoyancy generated by the heating would promote the shear layer development at the leading edge. The effect of buoyancy on the flow structure changes from leading edge to symmetry plane of the wing due to the existing velocity gradient that is also related with the forced and natural convection. At angles of attack $\alpha = 4°$ and $7°$, leading edge vortex pattern is apparent in the flow field for which the forced convection is presumed to be dominant for the uniform heat flux. For these cases, increasing the rate of uniform heat flux could not positively impact the flow field; instead it results in the movement of vortex core location slightly towards the symmetry plane and the decrease of the level of the vorticity contours. For $\alpha = 10°$, locally separated flow structure which could be the indication of pre-stall condition is observed, where the natural convection is expected to be influential as a result of the considerably low velocities existing on the wing. In line with this expectation, increasing the rate of uniform heat flux for $\alpha = 10°$ leads to the movement of the vortex core slightly towards the leading edge and increases the levels of the vorticity contours in the vicinity of the vortex core. However, a full recovery from stall condition cannot be obtained by performing the global heating from the wing surface, instead, local heating towards the leading edges of the wing may probably increase the effectiveness of the technique as stated in the recommendations for future work.

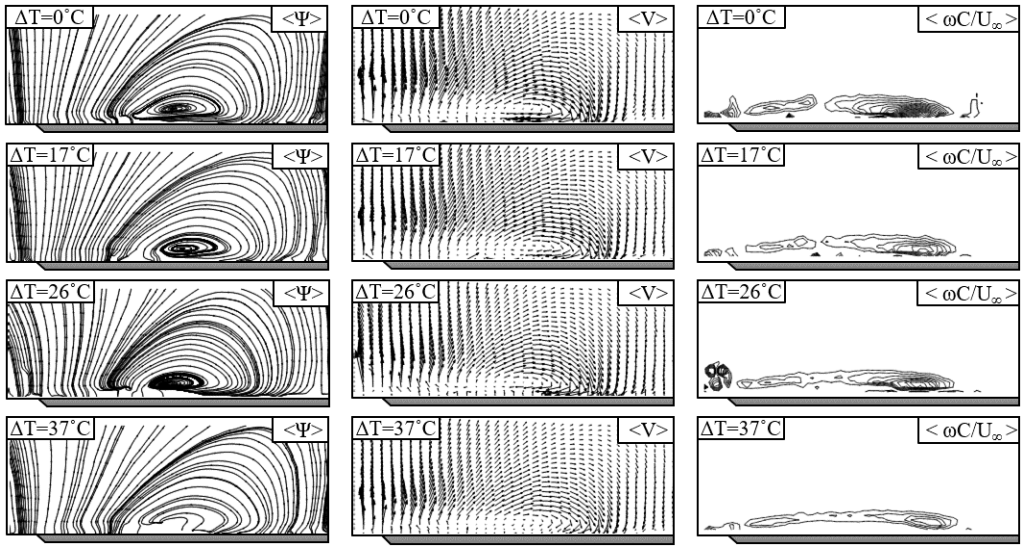


(a) (b) (c)

Figure 4.1 Comparison of (a) time-averaged streamline patterns, (b) velocity vector and (c) non-dimensional vorticity contours for zero (top row), low (second row), medium (third row) and high (bottom row) heat flux conditions at $Re = 3000$ and $\alpha = 4°$

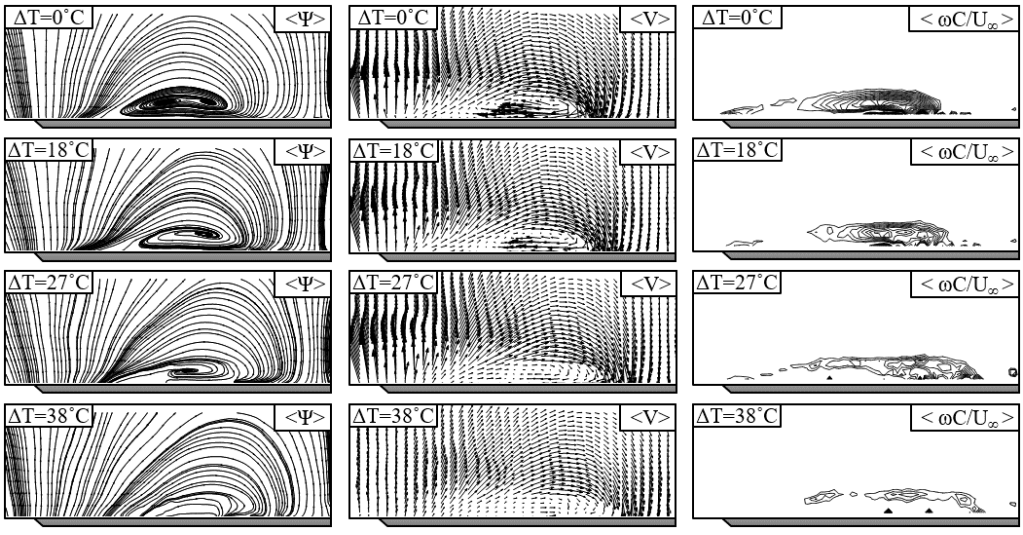


(a) (b) (c)

Figure 4.2 Comparison of (a) time-averaged streamline patterns, (b) velocity vector and (c) non-dimensional vorticity contours for zero (top row), low (second row), medium (third row) and high (bottom row) heat flux conditions at $Re = 3000$ and $\alpha = 7°$

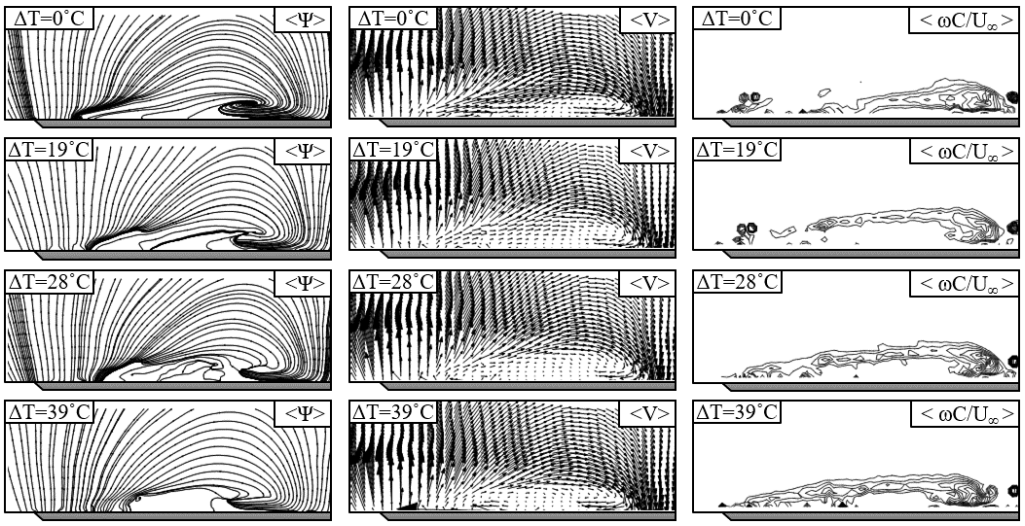


Figure 4.3 Comparison of (a) time-averaged streamline patterns, (b) velocity vector and (c) non-dimensional vorticity contours for zero (top row), low (second row), medium (third row) and high (bottom row) heat flux conditions at $Re = 3000$ and $\alpha = 10°$

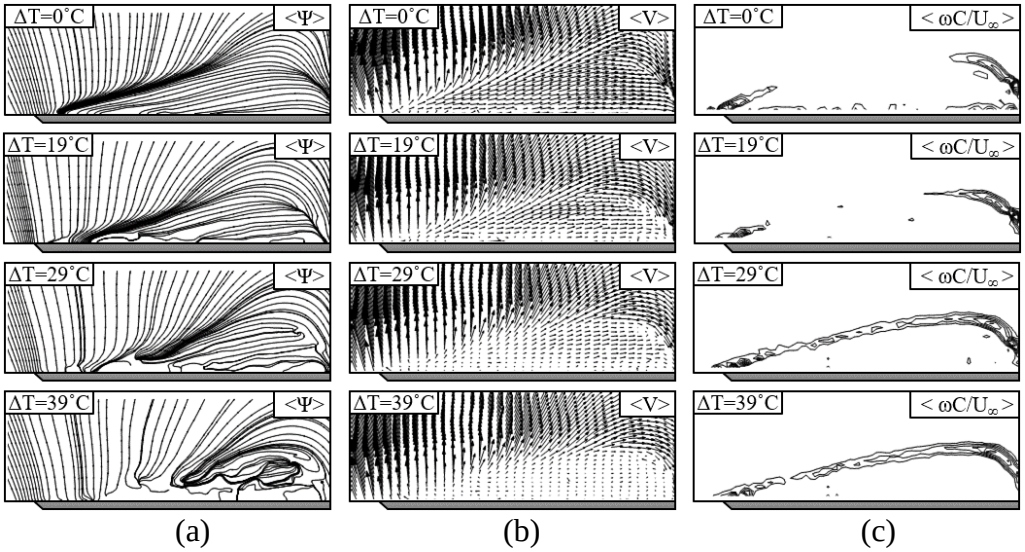


Figure 4.4 Comparison of (a) time-averaged streamline patterns, (b) velocity vector and (c) non-dimensional vorticity contours for zero (top row), low (second row), medium (third row) and high (bottom row) heat flux conditions at $Re = 3000$ and $\alpha = 13°$

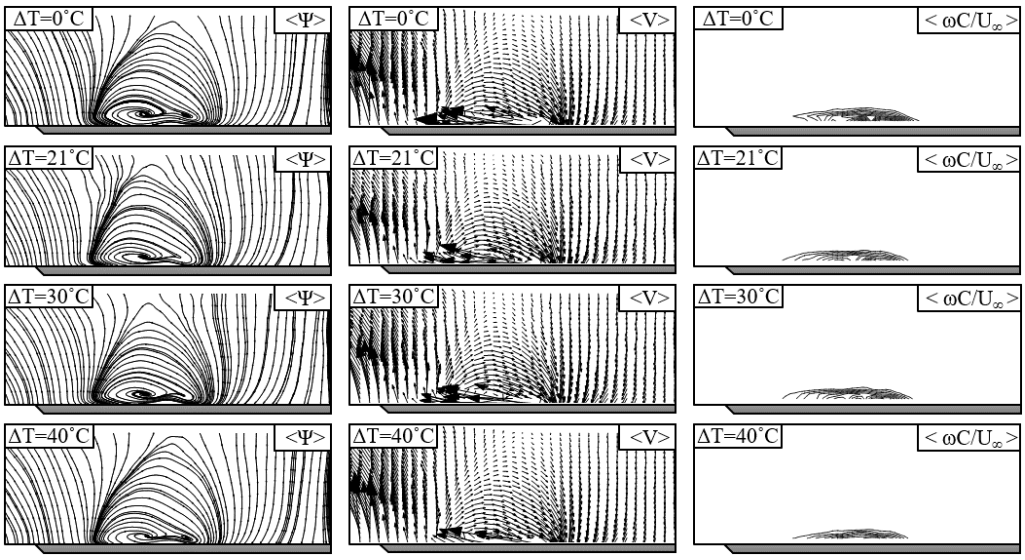


Figure 4.5 Comparison of (a) time-averaged streamline patterns, (b) velocity vector and (c) non-dimensional vorticity contours for zero (top row), low (second row), medium (third row) and high (bottom row) heat flux conditions at $Re = 8000$ and $\alpha = 4°$

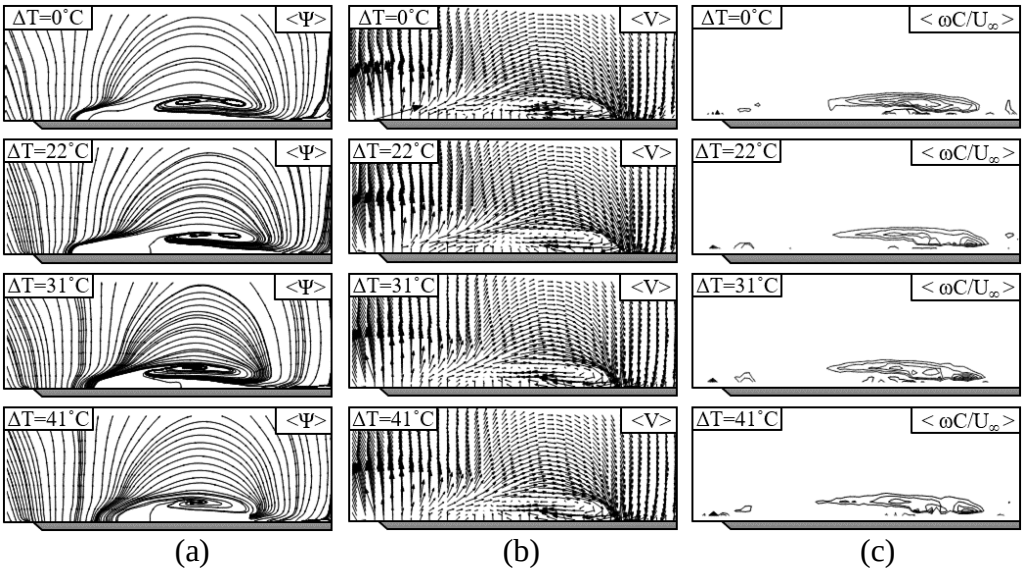


Figure 4.6 Comparison of (a) time-averaged streamline patterns, (b) velocity vector and (c) non-dimensional vorticity contours for zero (top row), low (second row), medium (third row) and high (bottom row) heat flux conditions at $Re = 8000$ and $\alpha = 7°$

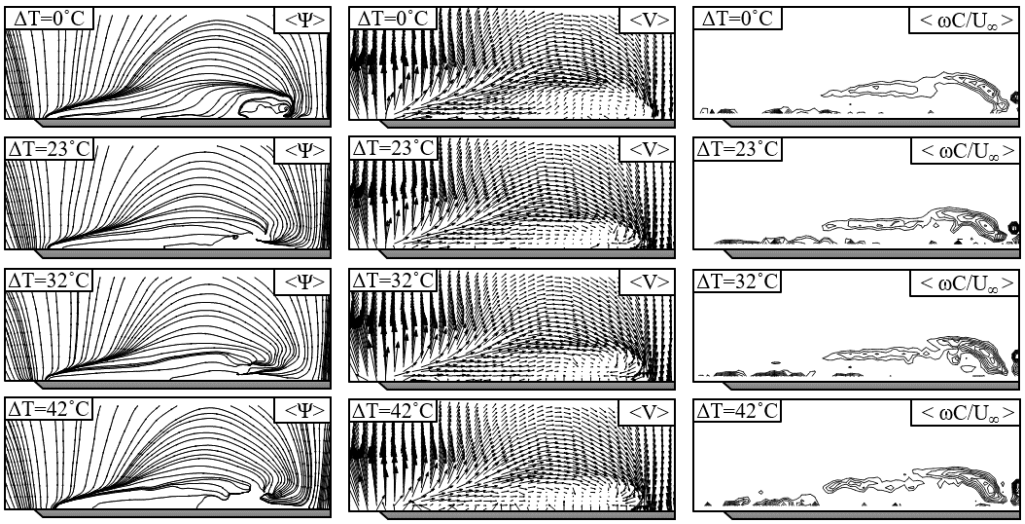


Figure 4.7 Comparison of (a) time-averaged streamline patterns, (b) velocity vector and (c) non-dimensional vorticity contours for zero (top row), low (second row), medium (third row) and high (bottom row) heat flux conditions at $Re = 8000$ and $\alpha = 10°$

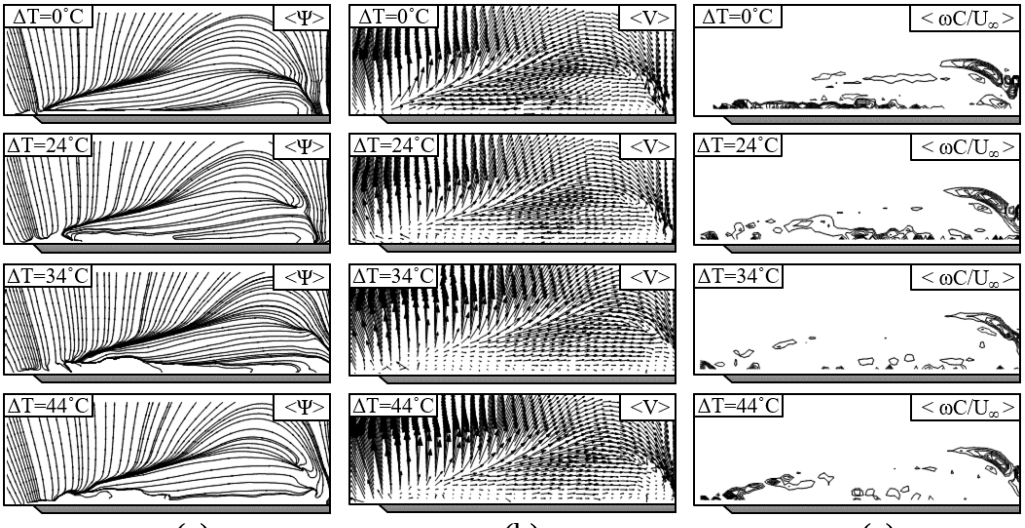


Figure 4.8 Comparison of (a) time-averaged streamline patterns, (b) velocity vector and (c) non-dimensional vorticity contours for zero (top row), low (second row), medium (third row) and high (bottom row) heat flux conditions at $Re = 8000$ and $\alpha = 13°$

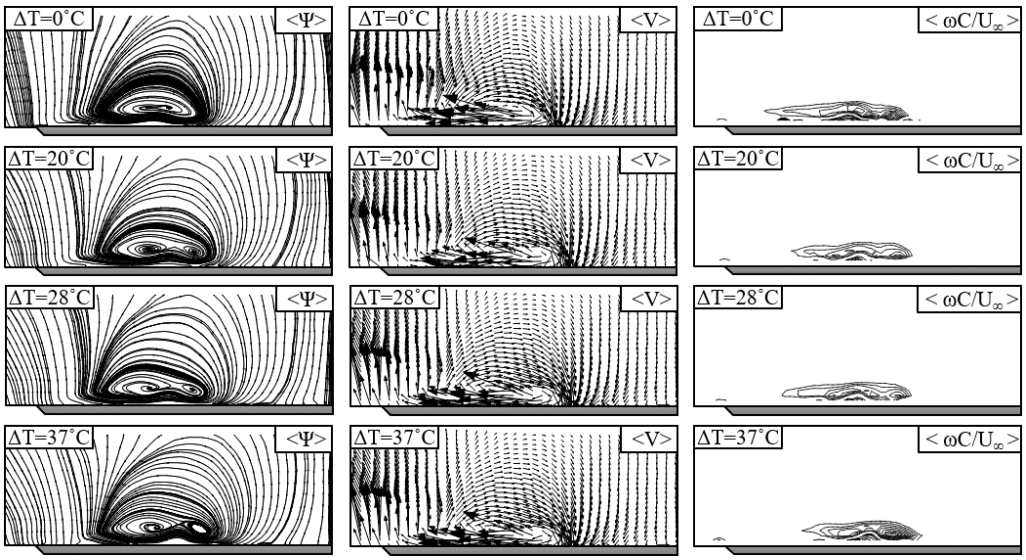


Figure 4.9 Comparison of (a) time-averaged streamline patterns, (b) velocity vector and (c) non-dimensional vorticity contours for zero (top row), low (second row), medium (third row) and high (bottom row) heat flux conditions at $Re = 10000$ and $\alpha = 4°$

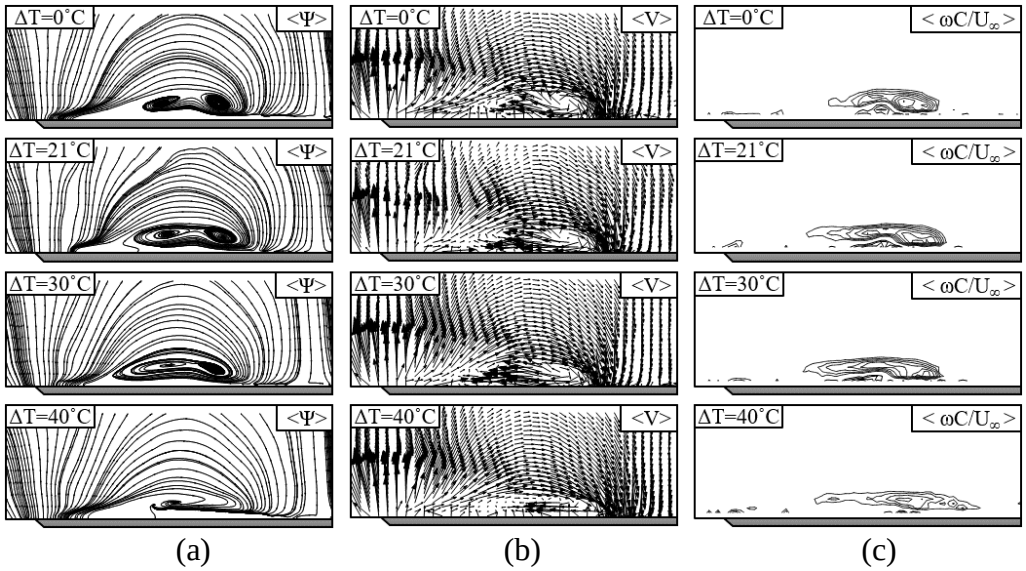


Figure 4.10 Comparison of (a) time-averaged streamline patterns, (b) velocity vector and (c) non-dimensional vorticity contours for zero (top row), low (second row), medium (third row) and high (bottom row) heat flux conditions at $Re = 10000$ and $\alpha = 7°$

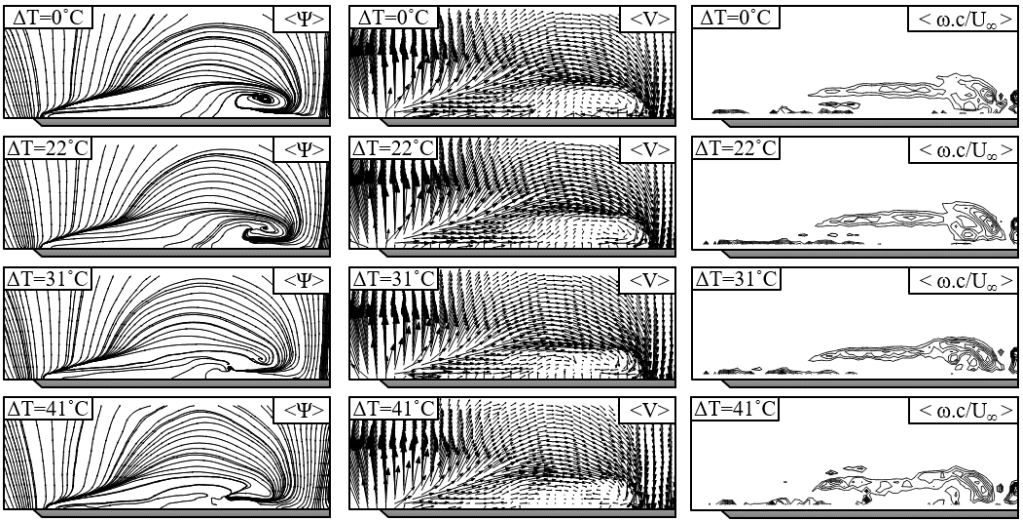


Figure 4.11 Comparison of (a) time-averaged streamline patterns, (b) velocity vector and (c) non-dimensional vorticity contours for zero (top row), low (second row), medium (third row) and high (bottom row) heat flux conditions at $Re = 10000$ and $\alpha = 10°$

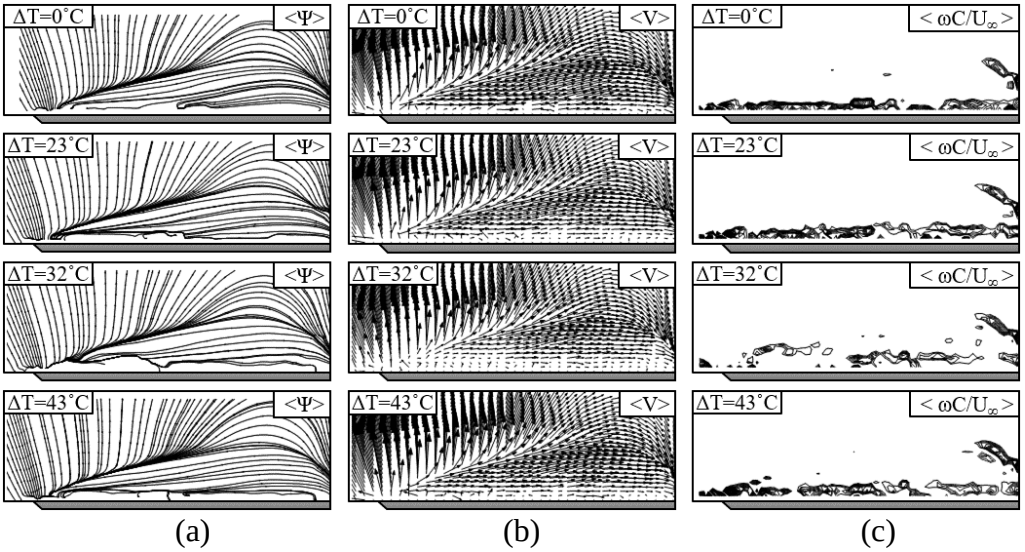


Figure 4.12 Comparison of (a) time-averaged streamline patterns, (b) velocity vector and (c) non-dimensional vorticity contours for zero (top row), low (second row), medium (third row) and high (bottom row) heat flux conditions at $Re = 10000$ and $\alpha = 13°$

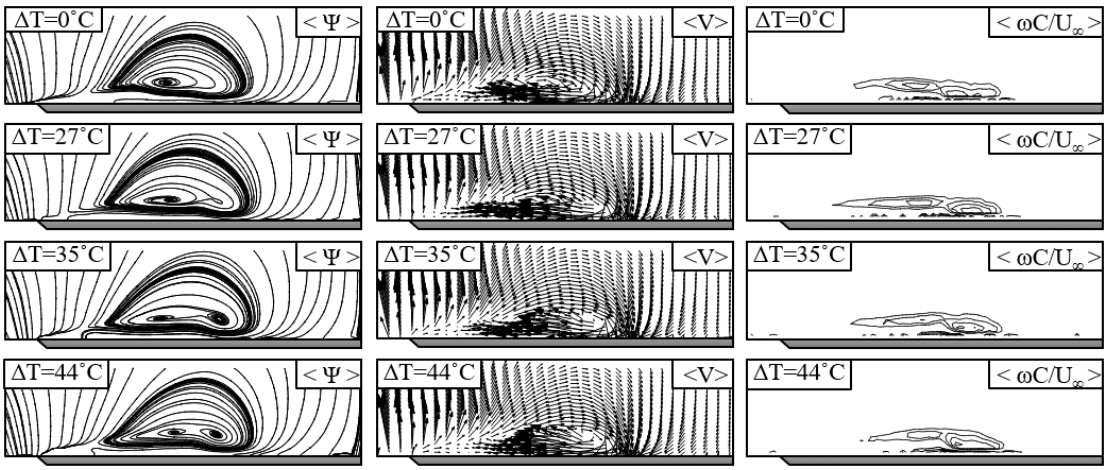


Figure 4.13 Comparison of (a) time-averaged streamline patterns, (b) velocity vector and (c) non-dimensional vorticity contours for zero (top row), low (second row), medium (third row) and high (bottom row) heat flux conditions at $Re = 20000$ and $\alpha = 4°$

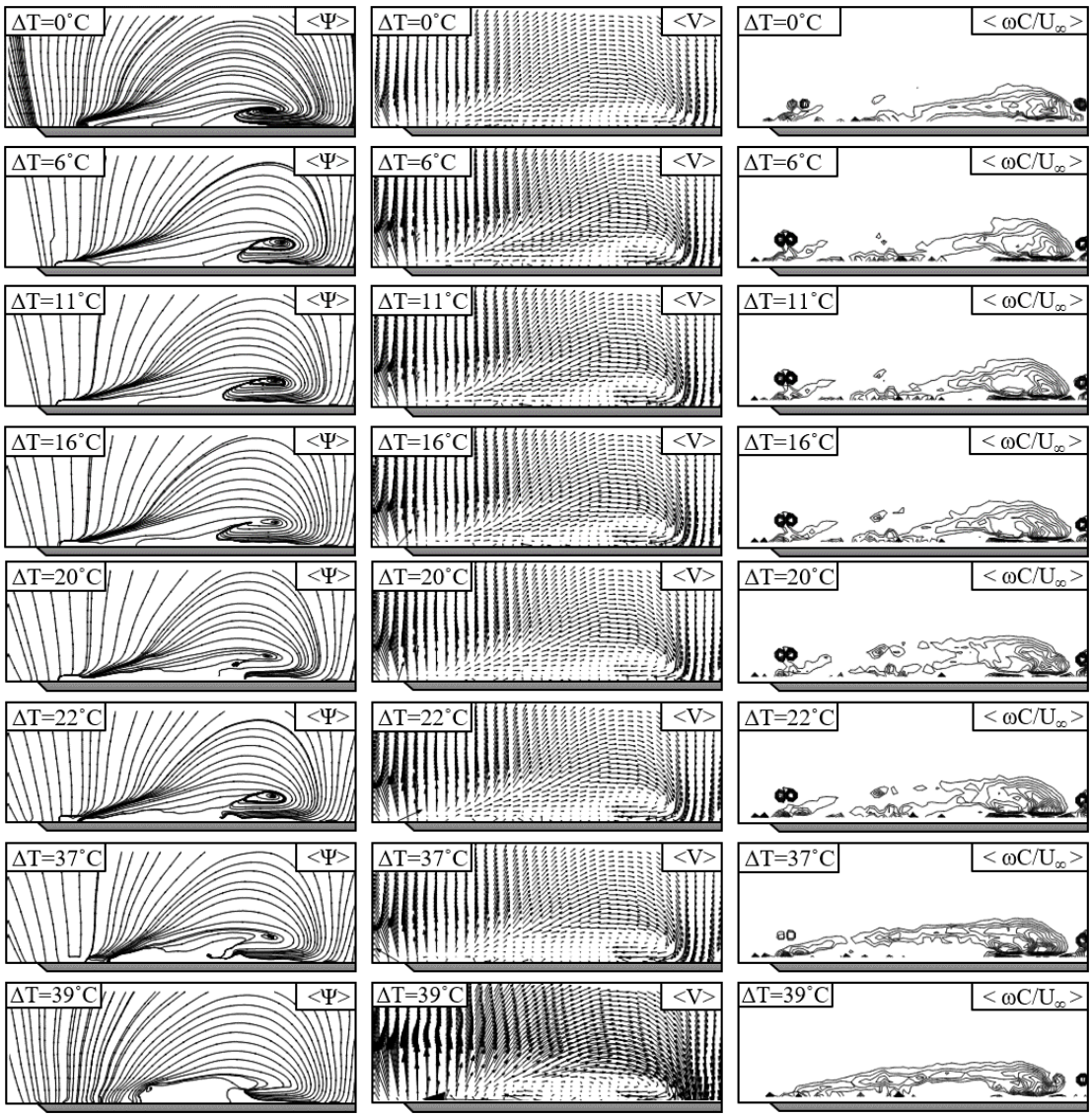


Figure 4.14 Comparison of (a) time-averaged streamline patterns, (b) velocity vector and (c) non-dimensional vorticity contours for transient period at $Re = 3000$ and $\alpha = 10°$

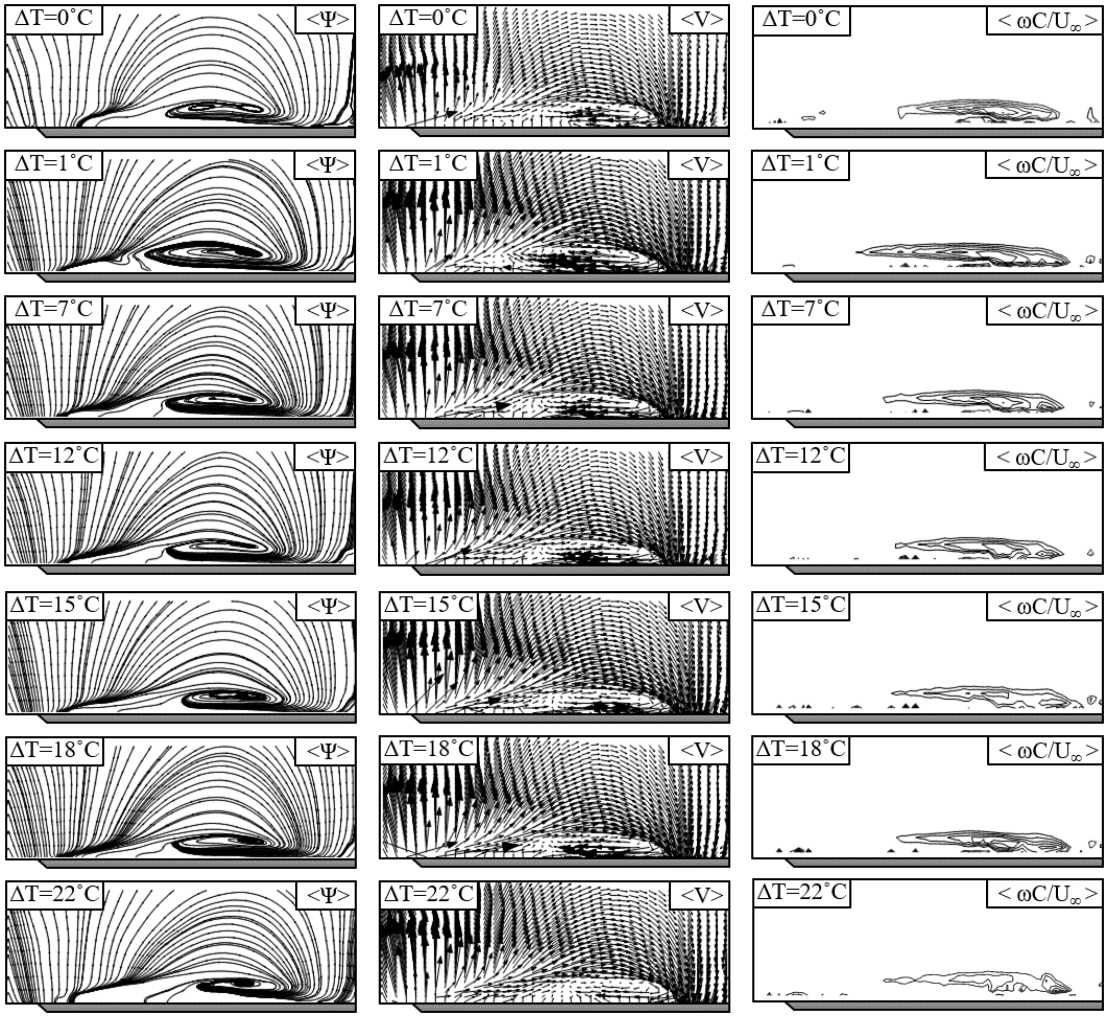


Figure 4.15 Comparison of (a) time-averaged streamline patterns, (b) velocity vector and (c) non-dimensional vorticity contours for transient period at $Re = 8000$ and $\alpha = 7°$

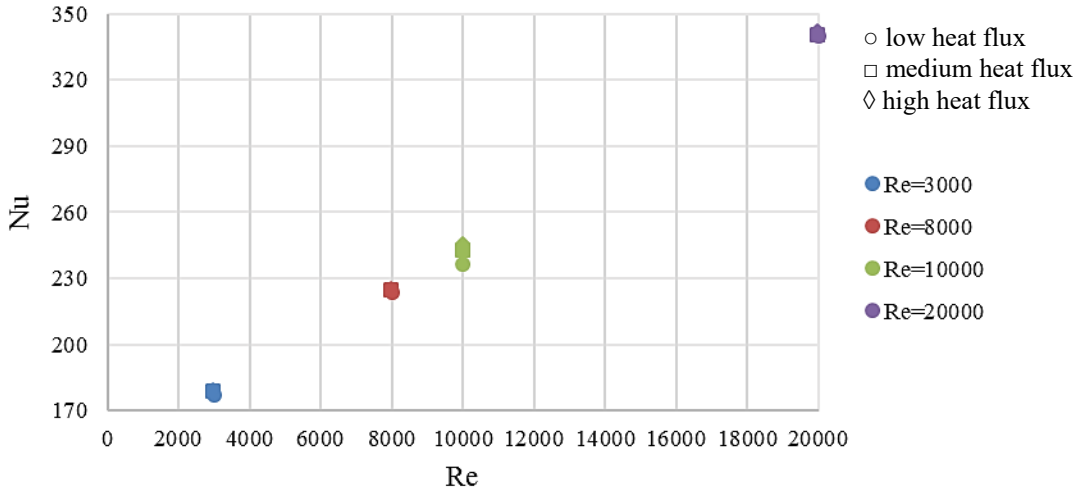


Figure 4.16 Nusselt number vs Reynolds number for angle of attack $\alpha = 4°$

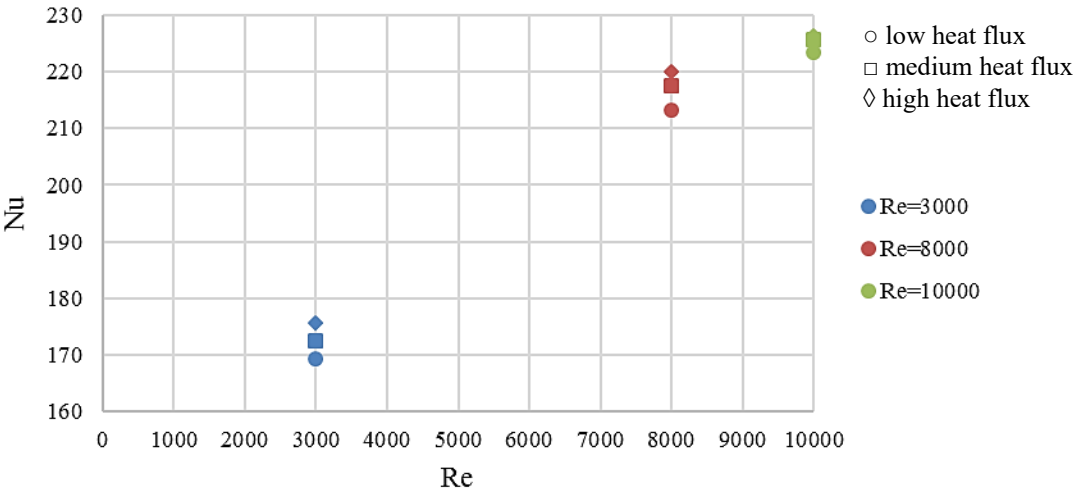


Figure 4.17 Nusselt number vs Reynolds number for angle of attack $\alpha = 7°$

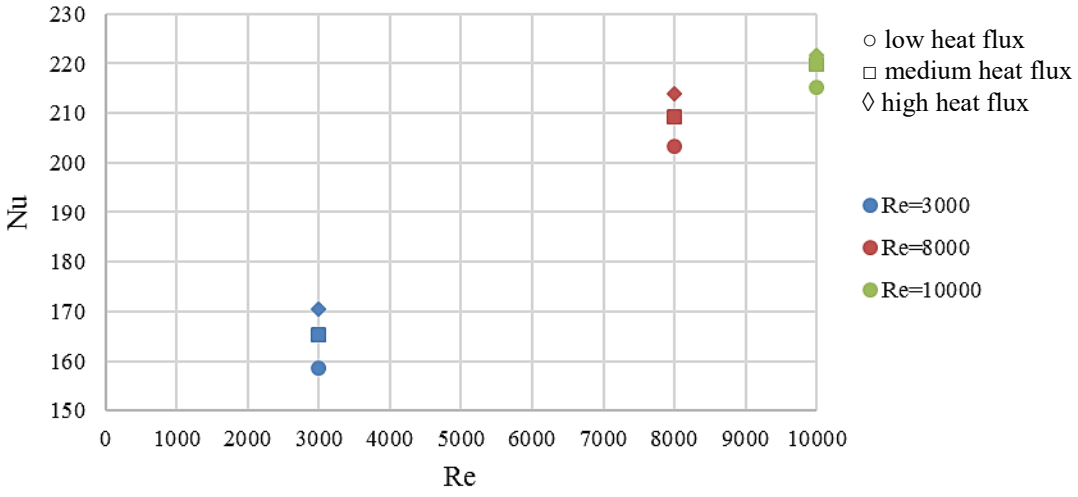


Figure 4.18 Nusselt number vs Reynolds number for angle of attack $\alpha = 10°$

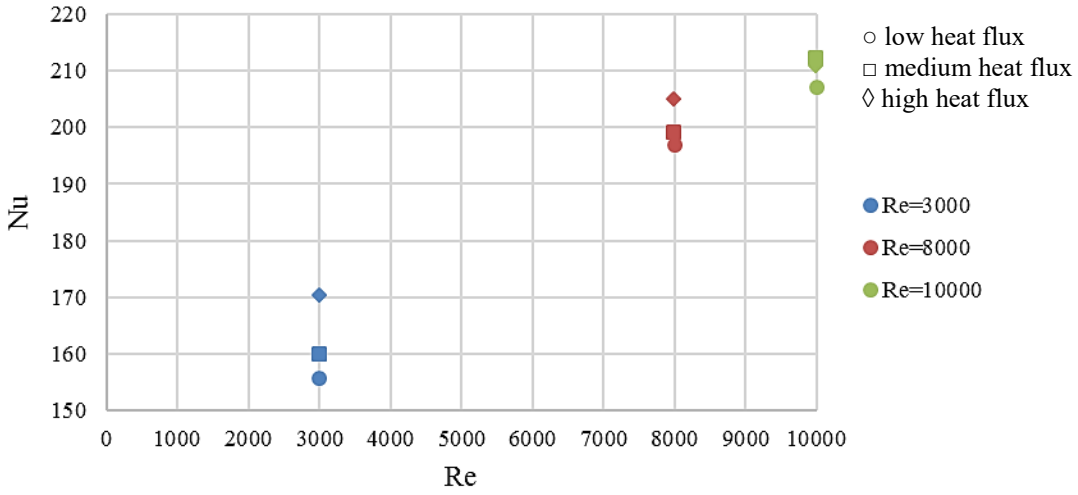


Figure 4.19 Nusselt number vs Reynolds number for angle of attack $\alpha = 13°$

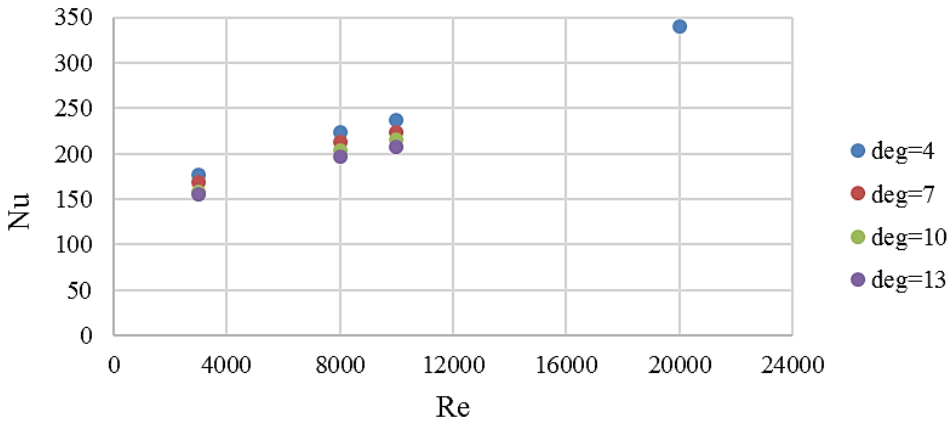


Figure 4.20 Nusselt number vs Reynolds number for low heat flux cases

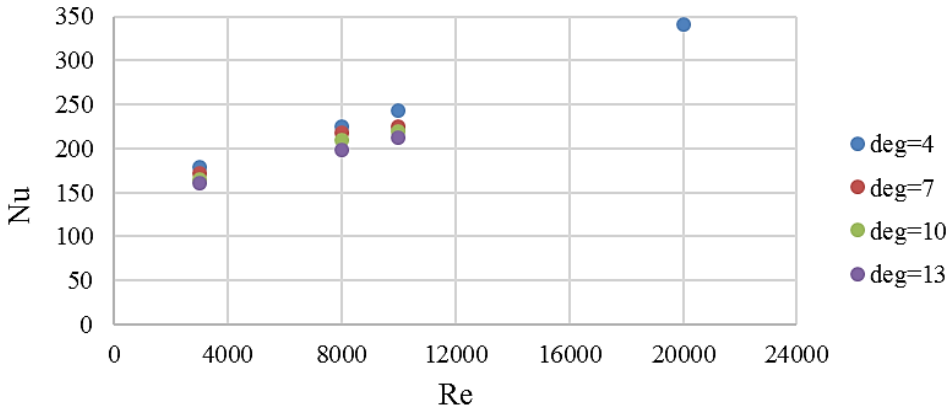


Figure 4.21 Nusselt number vs Reynolds number for medium heat flux cases

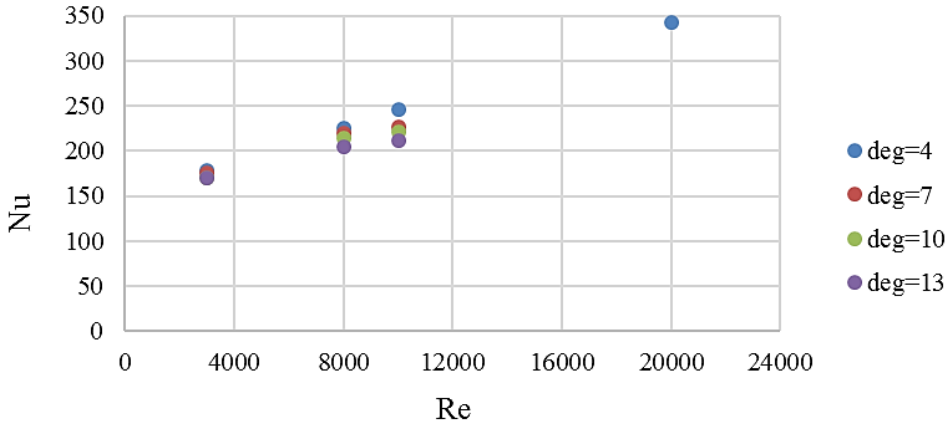


Figure 4.22 Nusselt number vs Reynolds number for high heat flux cases

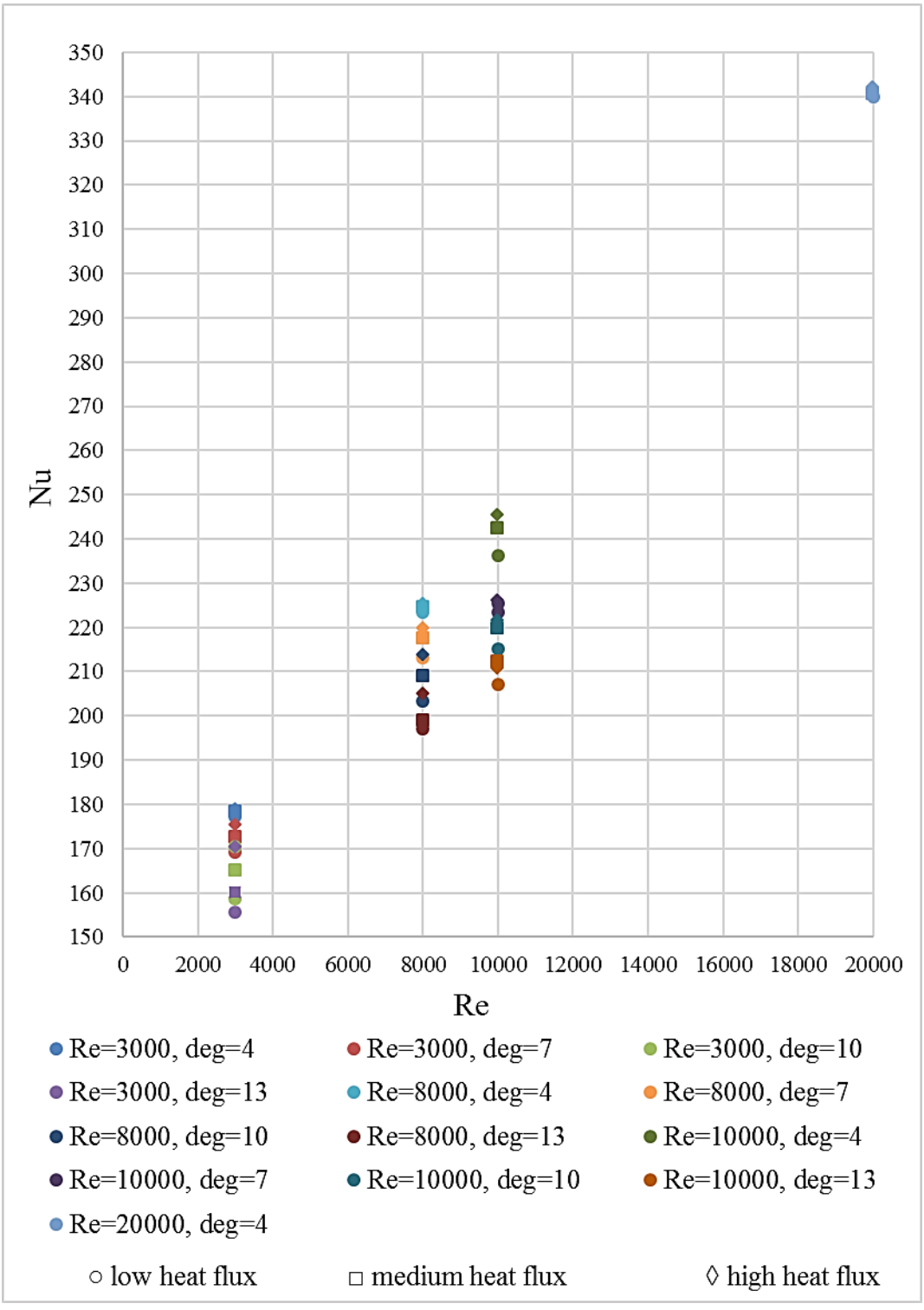


Figure 4.23 Nusselt number vs Reynolds number for experimental matrix

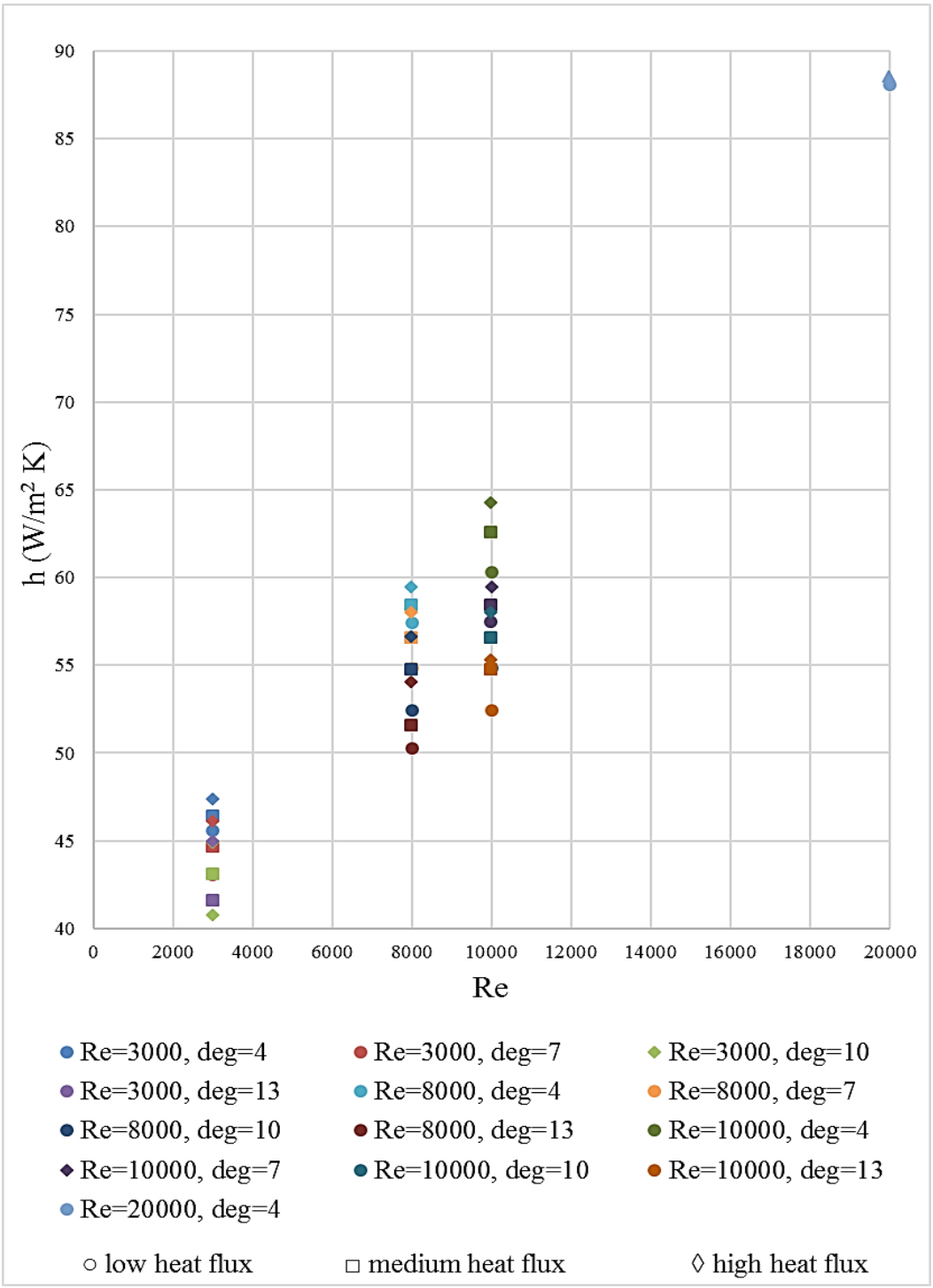


Figure 4.24 Heat transfer coefficient vs Reynolds number for experimental matrix

# CHAPTER 5

# CONCLUSION

## 5.1 Summary and Conclusions

The effect of thermal actuators on flow structure of a low swept delta wing with $\Lambda$=35$^o$ sweep angle was investigated experimentally in this study. First, the control test set-up, which was able to heat the wing surface and measure the surface temperature, was built. Then, the flow structure on the wing was quantified by using Particle Image Velocimetry (PIV) technique at Reynolds number of $Re = 3000, 8000$ and $10000$ for the attack angles of $\alpha = 4°, 7°, 10°$ and $13°$. Steady-state and transient heating condition were performed on the wing surface. Low, medium and high heat flux cases were applied as steady-state heating conditions.

According to the results of the current study, the following conclusions can be drawn for velocity measurements:

- Similar changes are obtained from no heat flux to high heat flux conditions at angles of attack $\alpha = 4°$ and $7°$ that leads to leading edge vortex pattern. Increasing the rate of uniform heat flux could not positively impact the flow field. According to the velocity vector and the vorticity contours, the location of the vortex core slightly moves towards the inboard of the symmetry plane with increase in heat flux. In addition, the level of the vorticity contours decreases from no heat flux to high heat flux conditions. In most cases, the velocity vectors show that, the magnitude of the velocity vectors also decreases by increasing heat flux.

- The effects of heat input on flow structure at angle of attack $\alpha = 10°$ are different compared to the results of attack angles $\alpha = 4°$ and $7°$. While leading edge vortex pattern is observed in the flow field for $\alpha = 4°$ and $7°$, pre-stall condition is obtained in the flow structure for attack angle $\alpha = 10°$. Natural convection appears to be dominant as a result of the considerably low velocities existing on the wing in pre-stall condition. The flow structure could be energized by heating the surface of the wing for which the buoyant forces are considered to be responsible. As a result of that, the vortex core slightly moves towards the leading edge when the heat input increases. In addition, the vorticity levels increase in the vicinity of the vortex core.
- The spatial extent of the vortex structure increases at $Re = 3000$ and $\alpha = 10°$ and $Re = 10000$ and $\alpha = 7°$. In addition, elongated shear layers from the leading edge of the wing were obtained for $Re = 3000$ and $\alpha = 10°$.
- For the transient period at $Re = 3000$ and $\alpha = 10°$, the vorticity contours show that, the level of the vorticity increases in the vicinity of the vortex core by increasing heat. The spatial extent of the vortex structure increases with observation of elongated shear layers from the leading edge of the wing. In addition, the reattachment location slightly shifts towards the leading edge.

The following conclusions can also be drawn for temperature measurements:

- Nusselt number increases at each angle of attack by increasing Reynolds number and increasing heat rate at all angles of attack except for $Re = 10000$ and $\alpha = 13°$. Nusselt number in medium heat flux condition is higher than high heat flux condition. In addition, Nusselt number reaches its highest value in the lowest angle of attack that corresponds to $\alpha = 4°$.
- Convective heat transfer coefficient also increases by increasing Reynolds

number and increasing heat rate for all cases at each angle of attack. In addition, by decreasing angle of attack, convective heat transfer coefficient increases for each Reynolds number.

## 5.2 Recommendations for Future Work

In this thesis, the effect of thermal actuators on flow structure of a low swept delta wing has been investigated experimentally. The present study can be further improved in the following ways:

- The current setup needs to be improved to test a wider range of Reynolds number and heat flux conditions. In addition, the seeding problems at high heat flux conditions need to be resolved.
- Near surface PIV measurements can be conducted to understand the effect of surface heating on the flow structure over the whole planform.
- Lift and drag force measurements can be performed to understand the effect of surface heating on the aerodynamic performance of the wing.
- Instead of global heating from the wing surface, the concept of local heat flux, such as heating towards the leading edges of the wing, can also be applied.

# REFERENCES


[1] I. Gursul, “Vortex flows on UAVs: Issues and challenges,” *Aeronaut. J.*, vol. 108, no. 1090, pp. 597–610, 2004.

[2] I. Gursul, Z. Wang, and E. Vardaki, “Review of Flow Control Mechanisms of Leading-edge Vortices,” *Prog. Aerosp. Sci.*, vol. 43, no. 7–8, pp. 246–270, 2007.

[3] I. Gursul, R. Gordnier, and M. Visbal, “Unsteady Aerodynamics of Nonslender Delta Wings,” *Prog. Aerosp. Sci.*, vol. 41, no. 7, pp. 515–557, 2005.

[4] G. S. Taylor and I. Gursul, “Buffeting Flows over a Low-Sweep Delta Wing,” *AIAA J.*, vol. 42, no. 9, pp. 1737–1745, 2004.

[5] I. Gursul, “Review of Unsteady Vortex Flows over Slender Delta Wings,” *J. Aircr.*, vol. 42, no. 2, pp. 299–319, 2003.

[6] P. B. Earnshaw and J. a Lawford, “Low-Speed Wind-Tunnel Experiments on a Series of Sharp-Edged Delta Wings,” *Aeronautical*, no. 3424, 1964.

[7] M. Zharfa, “Control of Flow Structure on Low Swept Delta Wing With Steady Leading Edge Blowing,” 2015.

[8] G. Bartlett, “Experimental Investigation of Influence of Edge Shape on the Aerodynamic Characteristics of Low Aspect Ratio Wings at Low Speeds,” *J. Aeronaut. Sci.*, vol. 22, no. 8, pp. 517–533, 1955.

[9] D. L. Kohlman and W. H. Wentz, JR., “Vortex Breakdown on Slender Sharp-edged Wings,” *J. Aircr.*, vol. 8, no. 3, pp. 156–161, Mar. 1971.

[10] M. Lee and C. M. Ho, “Lift Force of Delta Wings,” *Appl. Mech. Rev.*, vol. 43, no. 9, p. 209, 1990.

[11] T. Sarpkaya, “On Stationary and Travelling Vortex Breakdowns,” *J. Fluid Mech.*, vol. 45, no. 3, p. 545, Mar. 2006.

[12] T. Sarpkaya, “Vortex Breakdown in Swirling Conical Flows,” *AIAA J.*, vol. 9, no. 9, pp. 1792–1799, Sep. 1971.

[13] T. Sarpkaya, “Effect of the Adverse Pressure Gradient on Vortex Breakdown,” *AIAA J.*, vol. 12, no. 5, pp. 602–607, 1974.

[14] T. B. Benjamin, “Theory of the Vortex Breakdown Phenomenon,” *J. Fluid Mech.*, vol. 14, pp. 593–629, 1962.

[15] T. B. Benjamin, “Some Developments in the Theory of Vortex Breakdown,” *J. Fluid Mech.*, vol. 28, no. 1, pp. 65–84, 1967.

[16] M. G. Hall, “Vortex Breakdown,” *Annu. Rev. Fluid Mech.*, vol. 4, no. 1, pp. 195–218, 1972.

[17] M. Escudier, “Vortex breakdown: Observations and Explanations,” *Prog. Aerosp. Sci.*, vol. 25, no. 2, pp. 189–229, 1988.

[18] J. M. Delery, “Aspects of Vortex Breakdown,” *Prog. Aerosp. Sci.*, vol. 30, pp. 1–59, 1994.

[19] O. Lucca-Negro and T. O’doherty, “Vortex breakdown: A review,” *Prog. energy Combust. Sci.*, 2001.

[20] I. Gursul, “Unsteady Flow Phenomena over Delta Wings at High Angle of Attack,” *AIAA J.*, 1994.

[21] I. Gursul, “Review of Unsteady Vortex Flows over Slender Delta Wings,” *J. Aircr.*, vol. 42, no. 2, pp. 299–319, 2005.

[22] D. Rockwell, “Three-dimensional flow structure on delta wings at high angle-of-attack- Experimental concepts and issues,” *AIAA, Aerosp. Sci. Meet. Exhib. 31 st, Reno, NV*, p. 1993, 1993.

[23] R. E. Gordnier and M. R. Visbal, “Unsteady Vortex Structure over a Delta Wing,” *J. Aircr.*, vol. 31, no. 1, pp. 243–248, 1994.

[24] M. Menke, H. Yang, and I. Gursul, “Experiments on the Unsteady Nature of Vortex Breakdown over Delta Wings,” *Exp. Fluids*, vol. 27, no. 3, pp. 262–272, 1999.

[25] R. E. Gordnier and M. R. Visbal, “Higher-order Compact Difference Scheme Applied to the Simulation of a Low Sweep Delta Wing Flow,” *Aerosp. Sci. Meet. Exhib.*, no. January, 2003.

[26] O. K. Rediniotis, H. Stapountzis, and D. P. Telionis, “Vortex Shedding over Delta Wings,” *AIAA J.*, vol. 28, no. 5, pp. 944–946, 1990.

[27] M. Menke and I. Gursul, “Unsteady Nature of Leading Edge Vortices,” *Phys. Fluids*, vol. 9, no. 10, p. 2960, 1997.

[28] I. Gursul, “Origin of Vortex Wandering References,” *J. Aircr.*, vol. 37, no. 2, pp. 1996–1998, 1999.

[29] M. Menke and I. Gursul, “Self-excited Oscillations of Vortex Breakdown Location over Delta Wings,” *AIAA Pap.*, no. January, 1997.

[30] I. Gursul and H. Yang, “On Fluctuations of Vortex Breakdown Location,” *Phys. Fluids*, vol. 7, no. 1, p. 229, 1995.

[31] I. Gursul, “Buffeting Flows over Delta Wings,” *AIAA J.*, vol. 37, no. 2, p. 8, 1999.

[32] G. Taylor, T. Schnorbus, and I. Gursul, “An Investigation of Vortex Flows Over Low Sweep Delta Wings,” *AIAA Aerosp. Meet. Exhib.*, no. June, 2003.

[33] M. V. Ol and M. Gharib, “Leading-Edge Vortex Structure of Nonslender Delta Wings at Low Reynolds Number,” *AIAA J.*, vol. 41, no. 1, pp. 16–26, 2003.

[34] B. Yaniktepe and D. Rockwell, “Flow Structure on a Delta Wing of Low Sweep Angle,” *AIAA J.*, vol. 42, no. 3, pp. 513–523, 2004.

[35] M. Gad-El-Hak and R. F. Blackwelder, “Control of the Discrete Vortices from a Delta Wing,” *AIAA J.*, vol. 25, no. 8, pp. 1042–1049, 1987.

[36] F. M. Payne, T. T. Ng, R. C. Nelson, and L. B. Schiff, “Visualization and Wake Surveys of Vortical Flow over a Delta Wing,” *AIAA J.*, vol. 26, no. 2, pp. 137–143, 1988.

[37] M. Lowson, “The Three Dimensional Vortex Sheet Structure on Delta Wings,” *Fluid Dyn. Three-Dimensional Turbul. …*, 1988.

[38] R. Gordnier, “Computation of a Kelvin-Helmholtz Instability for Delta Wing Vortex Flows,” 1991.

[39] G. Reynolds and A. Abtahi, “Three-dimensional Vortex Development Breakdown, and Control,” *AIAA, 2nd Shear Flow Conf.*, 1989.

[40] T. Ng and D. Oliver, “Leading-edge Vortex and Shear Layer Instabilities,” *AIAA Pap.*, 1998.

[41] M. Visbal and R. Gordnier, “Origin of Computed Unsteadiness in the Shear Layer of Delta Wings,” *J. Aircr.*, 1995.

[42] M. Visbal and R. Gordnier, “On the Structure of the Shear Layer Emanating from a Swept Leading Edge at Angle of Attack,” *AIAA Pap.*, 2003.

[43] M. Yavuz, M. Elkhoury, and D. Rockwell, “Near-surface Topology and Flow Structure on a Delta Wing,” *AIAA J.*, 2004.

[44] G. Taylor and I. Gursul, “Unsteady Vortex Flows and Buffeting of a Low Sweep Delta Wing,” *AIAA Pap.*, 2004.

[45] G. Taylor and I. Gursul, “Buffeting Flows over a Low-Sweep Delta Wing,” *AIAA J.*, 2004.

[46] I. Gursul, E. Vardaki, P. Margaris, and Z. Wang, “Control of Wing Vortices,” *Notes Numer. Fluid Mech. Multidiscip. Des.*, vol. 95, pp. 137–151, 2007.

[47] A. Mitchell and J. Délery, “Research into Vortex Breakdown Control,” *Prog. Aerosp. Sci.*, 2001.

[48] S. Klute, R. Martin, O. Rediniotis, and D. Telionis, “Flow Control over Delta Wings at High Angles of Attack,” *AIAA Pap.*, 1993.

[49] R. Myose, S. Hayashibara, P. Yeong, and L. Miller, “Effect of Canards on Delta Wing Vortex Breakdown During Dynamic Pitching,” *J. Aircr.*, 1997.

[50] R. J. Lynn and I. Gursul, “Vortex Dynamics on a Generic UCAV Configuration,” *44th AIAA Aerosp. Sci. Meet. Exhib.*, no. January, 2006.

[51] E. Vardaki, I. Gursul, G. S. Taylor, and P. Student, “Physical Mechanisms of Lift Enhancement for Flexible Delta Wings,” *AIAA Pap.*, no. January, pp. 1–13, 2005.

[52] G. Taylor, A. Kroker, and I. Gursul, “Passive Flow Control over Flexible Non-Slender Delta Wings,” *AIAA Pap.*, no. January, pp. 1–17, 2005.

[53] G. Taylor, Z. Wang, E. Vardaki, and I. Gursul, “Lift Enhancement over Flexible Nonslender Delta Wings,” *AIAA J.*, vol. 45, no. 12, pp. 2979–2993, 2007.

[54] A. M. Mitchell, D. Barberis, P. Molton, and D. Jean, “Control of Leading-Edge Vortex Breakdown by Trailing Edge Injection Introduction,” *J. Aircr.*, vol. 39, no. 2, pp. 221–226, 2002.

[55] C. Shih and Z. Ding, “Trailing-edge Jet Control of Leading-edge Vortices of a Delta Wing,” *AIAA J.*, vol. 34, no. 7, pp. 1447–1457, 1996.

[56] S. Phillips, C. Lambert, and I. Gursul, “Effect of a Trailing-Edge Jet on Fin Buffeting Introduction,” *J. Aircr.*, vol. 40, no. 3, 2003.

[57] P. V Vorobieff and D. O. Rockwell, “Vortex Breakdown on Pitching Delta Wing: Control by Intermittent Trailing-edge Blowing,” *Aiaa J.*, vol. 36, no. 4, pp. 585–589, 1998.

[58] D. Hummel, “Zur Umströmung scharfkantiger schlanker Deltaflügel bei großen Anstellwinkeln,” *Z. Flugwiss*, 1967.

[59] J. Wang, Q. Li, and J. Liu, “Effects of a Vectored Trailing Edge Jet on Delta Wing Vortex Breakdown,” *Exp. Fluids*, 2003.

[60] D. Nawrocki, “Differential and Vectored Trailing Edge Jet Control of Delta Wing Vortices,” *AIAA Pap.*, 1995.

[61] B. Badran and S. Mccormick, “Control of Leading-Edge Vortices with Suction,” *J. Aircr.*, vol. 35, no. 1, pp. 163–165, 1997.

[62] S. McCormick and I. Gursul, “Effect of Shear-layer Control on Leading-edge Vortices,” *J. Aircr.*, vol. 33, no. 6, pp. 1087–1093, 1996.

[63] B. H. Maines, B. Moeller, and O. K. Rediniotis, “The Effects of Leading Edge Suction on Delta Wing Vortex Breakdown,” *AIAA, Aerosp. Sci. Meet. Exhib.* , no. c, 1999.

[64] N. J. Wood, L. Roberts, and Z. Celik, “Control of Asymmetric Vortical Flows over Delta Wings at High Angles of Attack,” *J. Aircr.*, vol. 27, no. 5, pp. 429–435, 1990.

[65] M. Gad-El-Hak and R. F. Blackwelder, “Control of the Discrete Vortices from a Delta Wing,” *AIAA J.*, vol. 25, no. 8, pp. 1042–1049, 1987.

[66] W. Gu, O. Robinson, and D. Rockwell, “Control of Vortices on a Delta Wing by Leading-edge Injection,” *AIAA J.*, vol. 31, no. 7, pp. 1177–1186, 1993.

[67] D. Greenwell and N. Wood, “Roll Moment Characteristics of Asymmetric Tangential Leading-edge Blowing on a Delta Wing,” *J. Aircr.*, vol. 31, no. 1, pp. 161–168, 1994.

[68] Y. D. Cui, T. T. Lim, and H. M. Tsai, “Control of Vortex Breakdown over a Delta Wing Using Forebody Spanwise Slot Blowing,” *AIAA J.*, vol. 45, no. 1, pp. 110–117, 2007.

[69] Y. D. Cui, T. T. Lim, and H. M. Tsai, “Forebody Slot Blowing on Vortex Breakdown and Load Over a Delta Wing,” *AIAA J.*, vol. 46, no. 3, pp. 744–751, 2008.

[70] Q. Deng and I. Gursul, “Effect of leading-edge flaps on vortices and vortex breakdown,” *Exp. Fluids*, vol. 23, no. 4, pp. 347–352, 1996.

[71] Z. Wang, P. Jiang, and I. Gursul, “Effect of Thrust-Vectoring Jets on Delta Wing Aerodynamics,” *J. Aircr.*, vol. 44, no. 6, pp. 1877–1888, 2007.

[72] P. Jiang, Z. Wang, and I. Gursul, “Effects of Unsteady Trailing-Edge Blowing on Delta Wing Aerodynamics,” *J. Aircr.*, vol. 47, no. 2, pp. 591–602, 2010.

[73] M. Yavuz and D. Rockwell, “Control of Flow Structure on Delta Wing with Steady Trailing-Edge Blow,” *AIAA J.*, vol. 44, no. 3, pp. 493–501, 2006.

[74] E. Vardaki, Z. Wang, and I. Gursul, “Flow Reattachment and Vortex Re-formation on Oscillating Low-Aspect-Ratio Wings,” *AIAA J.*, vol. 46, no. 6, pp. 1453–1462, 2008.

[75] N. Williams, Z. Wang, and I. Gursul, “Active Flow Control on a Nonslender Delta Wing,” *J. Aircr.*, 2008.

[76] J. MARCHMAN and III, “Effect of Heating on Leading Edge Vortices in Subsonic Flow,” *J. Aircr.*, vol. 12, no. 2, 1975.

[77] D. J. Norton, J. M. Macha, and J. C. Young, “Surface Temperature Effect on Subsonic Stall,” *J. Spacecr. Rockets*, vol. 10, no. 9, pp. 581–587, Sep. 1973.

[78] D. G. Mabey, “Effects of heat transfer on aerodynamics and possible implications for wind tunnel tests,” *Prog. Aerosp. Sci.*, vol. 27, no. 4, pp. 267–303, Jan. 1990.

[79] G. J. Balle and R. E. Breidenthal, “Stationary Vortices and Persistent Turbulence in Karman Grooves,” *J. Turbul.*, vol. 3, p. N33, Jan. 2002.

[80] S. Srigrarom and N. Lewpiriyawong, “Effect of Stationary Vortex to Heat Transfer on Delta Wings,” *Int. Congr. Aeronaut. Sci.*, 2004.

[81] J. Kim, Z. Rusak, and N. Koratkar, “Small-scale Airfoil Aerodynamic Efficiency Improvement by Surface Temperature and Heat Transfer,” *AIAA J.*, 2003.

[82] N. Bekka and R. Bessaih, “Numerical study of heat transfer around the small scale airfoil using various turbulence models,” *Numer. Heat Transf. …*, 2009.

[83] A. J. Wheeler and A. R. Ganji, “Experimental Uncertainty Analysis,” *Introd. to Eng. Exp.*, vol. 3rd ed. Ne, pp. 199–237, 2010.

[84] “Measurement Principles of PIV.” [Online]. Available: http://www.dantecdynamics.com/measurement-principles-of-piv.

# APPENDIX

## SAMPLE CALCULATION ABOUT TEMPERATURE MEASUREMENTS

In this appendix, sample calculations of heat transfer coefficient ($h$) and Nusselt number ($Nu$) with respect to the temperature measurements are given step-by-step. $Re = 3000, \alpha = 4°$ low heat flux condition is selected as a representative case. The voltage value for the selected case is 20 V with current 0.610 A. The area of the wing surface is 0.016 m$^2$. According to all data, the heat flux for this case can be as following.

$$q" = \frac{V \cdot I}{A} \tag{B.1}$$

$$q" = \frac{20 \cdot 0.610}{0.016} = 774.6\ (W/m^2)$$

The convective heat transfer coefficient can be calculated as following

$$h = \frac{q"}{\Delta T} \tag{B.2}$$

The heated wing surface is at $T_s = 46°C$ and the ambient temperature is $T_\infty = 29°C$. Thus, the difference in temperature is $\Delta T = 17°C$.

$$h = \frac{q"}{\Delta T} = \frac{774.6}{17} = 45.565\ (W/m^2K)$$

$$T_f = \frac{T_s + T_\infty}{2} \tag{B.3}$$

$$T_f = \frac{46 + 29}{2} = 37.5\ [℃]$$

By using the obtained film temperature, the thermal conductivity of air is found as $k = 0.027\ (W/mK)$ . [88] The characteristic length of the wing correspond to the chord length equal to $0.105$ m. Therefore, Nusselt number is as follows.

$$Nu = \frac{h \cdot C}{k} \tag{B.4}$$

$$Nu = \frac{45.565 \cdot 0.105}{0.027} = 177.2$$